Summer 2024

The Geodetic Strain Rates from Gnss in the North American-Carribean-Cocos Triple Junction in Guatemala and Implications for Seismic Hazard

Tanaya Kashyap
Missouri University of Science and Technology

Department:

THE GEODETIC STRAIN RATES FROM GNSS IN THE NORTH AMERICAN-CARRIBEAN-COCOS TRIPLE JUNCTION IN GUATEMALA AND IMPLICATIONS FOR SEISMIC HAZARD

by

TANAYA KASHYAP

A THESIS

Presented to the Graduate Faculty of the

MISSOURI UNIVERSITY OF SCIENCE AND TECHNOLOGY

In Partial Fulfillment of the Requirements for the Degree

MASTER OF SCIENCE IN GEOLOGY AND GEOPHYSICS

2024

Approved by:

Jeremy Maurer, Advisor
Jonathan Obrist-Farner
Andreas Eckert

ABSTRACT

Geodetic velocity data are pivotal for deciphering seismic risks, providing initial constraints for crustal surface strain rates. Gaining an understanding of the 2D surface strain tensor across an entire area necessitates knowledge of the surface velocity field, yet geodetic data such as measurements from the Global Navigation Satellite System (GNSS) are dispersed across the Earth's surface. In the current scope of study, we have employed various methodologies to estimate strain rates in Guatemala, utilizing GNSS velocity data and leveraging the open-source Python tool Strain_2D. Strain_2D facilitates the computation of strain rates through diverse methods applied to the same dataset and grid. Three distinct interpolation approaches were incorporated to compute strain rates, aiming to quantify uncertainty and achieve more reliable outcomes. This study determined that the selection of parameters profoundly affects the strain rate field and utilized the L-curve technique to assess the balance between fitting the data and minimizing unnecessary strain signals. The findings indicate that the maximum shear strain distinctly outlines the triple junction (Cocos-North America-Caribbean) within the Guatemala City Graben, aligning with findings from previous research. Results indicate moment rates between of 2.88×10^{18} N m/yr and 4.72×10^{18} N m/yr depending on the method used. An average data misfit of 0.5 to 0.6 is also observed.

ACKNOWLEDGMENTS

I would like to express my sincere gratitude to the following individuals.

Dr. Jeremy Maurer and Dr. Jonathan Obrist-Farner, for providing me with the opportunity to work on this thesis and for their guidance and mentorship throughout the process. Dr. Andreas Eckert for giving me valuable comments and guidance as my committee. Everyone in the GEM-lab who have provided me with valuable feedback and support. Finally, my friends and family for their unvarying belief in me.

TABLE OF CONTENTS

Page

LIST OF ILLUSTRATIONS

LIST OF TABLES

NOMENCLATURE

Symbol	Description
CO	Cocos Plate
NA	North American Plate
CA	Caribbean Plate
MAT	Middle America Trench
PMFZ	Polochic Motagua Fault Zone
CAVA	Central American Volcanic Arc
PF	Polochic Fault
MF	Motagua Fault
JOF	Jocotán Fault
M_w	Magnitude
I_2	Second Invariant of the strain tensor
ESFZ	El Salvador Fault Zone
ε	Strain
λ	Vector of Kriging weights

1. INTRODUCTION

Geodetic data constrain the present-day accumulation of tectonic strain. This accumulation is expected to be released primarily through earthquakes, making such data a valuable source for gaining insights into potential seismic risks in the future. Further, geodetically derived strain rates can constrain fault activity, which is independent of geological and paleoseismological estimates. This study will be using GNSS data to understand strain accumulation between the North American, Caribbean and Cocos plates. It will quantify strain accumulation on and around the Polochic-Motagua Fault System (PMFS) and strike-slip faults along the Central America Volcanic Arc (CAVA). Additionally, it will model fault slip rates and locking depths based on these calculated strain rates. This research aims to answer several key questions, including the identification of active faults, in particular which faults are active in the PMFS, and determining the moment accumulation rates on the faults in the PMFS. Furthermore, the study seeks to explore the implications of the findings on seismic hazard, thereby contributing insights to seismic preparedness in the region.

1.1. BACKGROUND

1.1.1. Regional Tectonic Context. The PMFS forms the northwesternmost portion of the CA-NA plate boundary, while the strike-slip faults of the CAVA form the westernmost portion of the CA-CO plate boundary. The entire region behaves as a diffuse triple junction of three tectonic plates: the Cocos plate (CO), the North American Plate (NA), and finally the Caribbean plate (CA) (Figure 1.1). The CO plate is subducting

beneath the NA and CA plates in the eastern Pacific Ocean off the coast of Mexico and Central America along the Middle America Trench (MAT), giving rise to the Central America Volcanic Arc (CAVA). Strike-slip faulting along the CAVA has given rise to a forearc sliver of crust that is translating northwest and may be sutured to the NA plate (Álvarez-Gómez et al., 2019). The boundary between the NA and CA plates is the complex left-lateral transform fault system, the Polochic-Motagua Fault System (PMFS), while the Guatemala City Graben and other faults in the central Basin-and-Range province accommodate extension in central Guatemala; in particular, this study will show that the Guatemala City Graben links the two transform fault systems (Garnier et al., 2022).

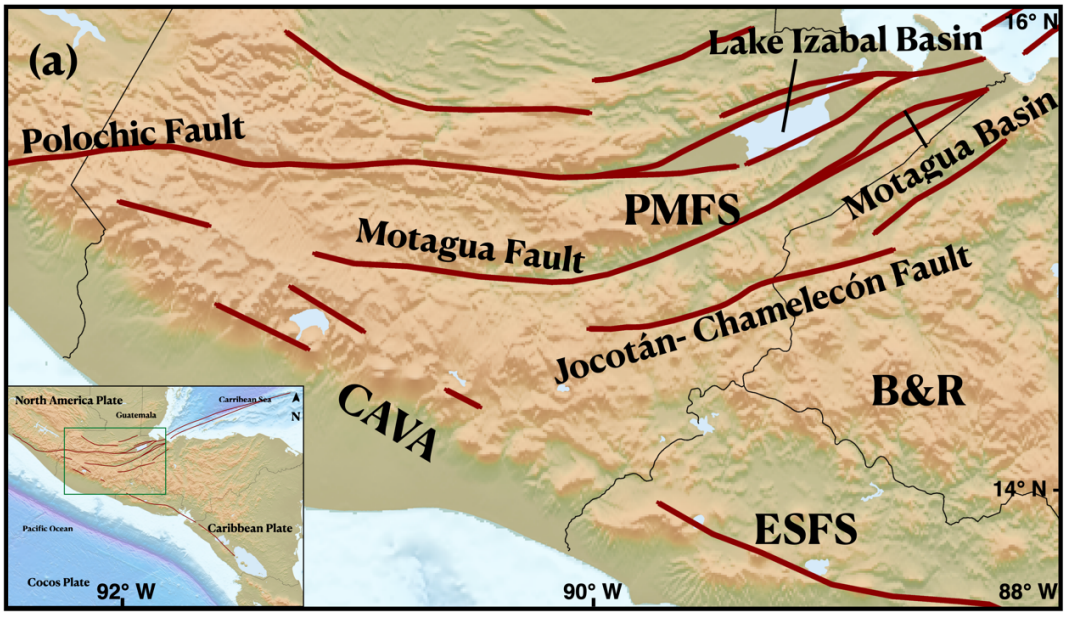

Figure 1.1 Tectonic setting of the PMFS, CAVA, and the triple junction. Plate tectonic setting of the Caribbean (CA) plate, the Cocos (CO) plate, and the North American (NA) plate. The green bounding box in the reference picture is the area of study and the red lines are the fault lines. The NA-CA plate boundary forms the PMFS. The western CA plate forms a Basin and Range (B&R) province due to extension from pinning between the NA and the CO plates. North of the PMFS, folding and thrusting results from the NA-CO convergence. A crustal sliver between the CAVA and the CO plate accommodates trench-parallel motion between the CO-CA plates.

1.1.2. Seismicity of the Region. The PMFS has experienced several large historic earthquakes, including the 1976 M_W7.6 Motagua Fault earthquake (Plafker, 1976; Kanamori & Stewart, 1978). White (1984) studied the history of seismicity in the Guatemala region, including the epicenter of earthquakes, magnitudes, and damages. In 1785, an earthquake with M_w 7.3-7.5 ruptured the eastern part of the Polochic fault (PF), while the the western PF, adjacent to the location of the 1785 event, ruptured in 1816 with a M_w 7.5-7.7 (White, 1984). The 1976 Motagua earthquake ruptured the MF for ~230 km, killed ~23,000 people and left 1.5 million people homeless (Plafker, 1976; Olcese et al., 1977). All these events caused casualties and major damage to buildings. Figure 1.2 shows modern seismicity, distributed primarily along the subduction zone and Swan Fault offshore eastern Guatemala, with some events along the transform faults of the PMFS and CAVA.

1.2. FAULTS IN THE PMFS

There are three roughly parallel, strike-slip, left lateral faults included in the PMFS: the Polochic Fault (PF), the Motagua Fault (MF), and the Jocotan Fault (JOF) (Figure 1.1). It has been proposed that the PF extends ~400km on land and has experienced ~130 km offset (Buraket, 1978) since the Neogene, forming a large pull-apart basin called the Izabal Basin that is estimated to have ~4km of sediments (Lodolo et al., 2009). The MF extends ~300km and is thought be some authors to have experienced ~300km of displacement since the Neogene (e.g., Ratschbacher et al., 2009), creating the Motagua Valley, which has ~1km of sediments (Lodolo et al., 2009). The JOF is located south of the other faults in the

system and has a length of ~200km. Collectively, these are known as the Polochic-Motagua Fault System (PMFS).

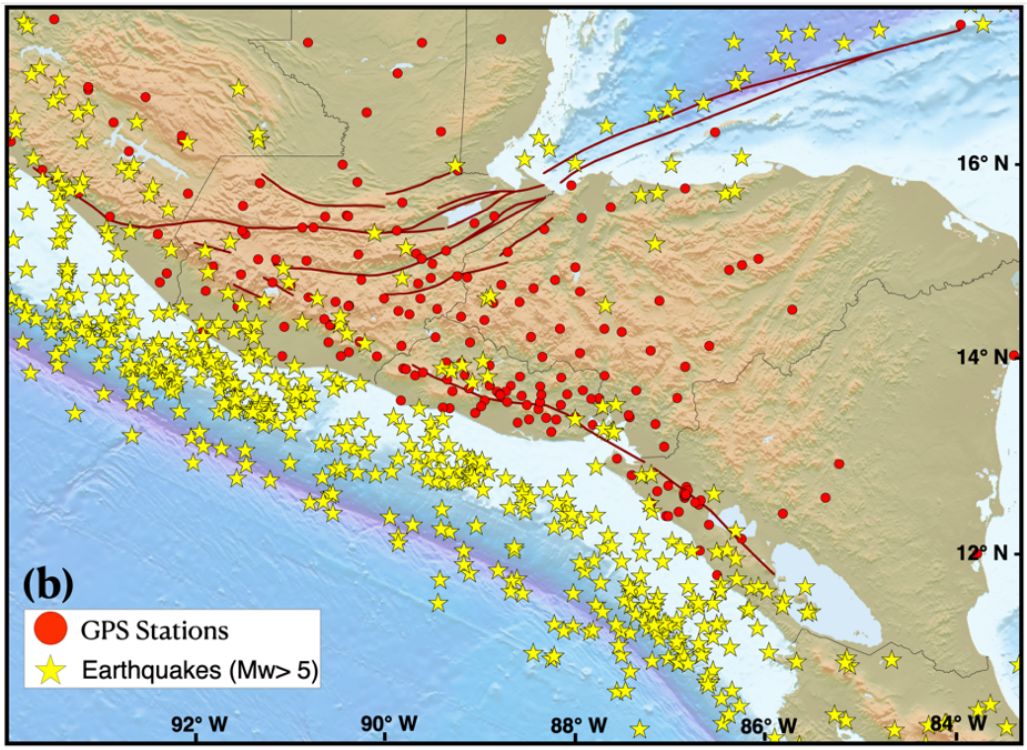

Figure 1.2 Seismicity from the global CMT moment tensor database. The red circles are the GNSS stations both continuous and campaign data (Ellis et al. 2019) and the yellow stars are the seismic events of M_w 5 and greater in the study area. The magenta lines are the faults in the study area.

The MF is the largest geologic structure in Guatemala, running along the Motagua river valley. The fault is clearly visible in aerial photography and satellite imagery. During the February 4, 1976 earthquake, this fault was displaced up to 2m (average ~1.1m; Buckman, 1978), with a rupture length of ~230km (Plafker, 1976; Kanamori & Stewart, 1978; Langer & Bollinger 1978; Young et al., 1989).

Contemporary tectonic analysis of the PF suggests that it is currently a minor fault of the plate boundary compared to the MF (Ellis et al., 2019; Franco et al., 2012, Authemayou et al., 2012). Guzmán-Speziale (2010) found seismicity in the zone north of the PF. (Bonis et al. 1970; Case & Holcombe, 1980; Weyl, 1980; French & Schenk, 2004). The PF likely had a larger slip rate in the past (Authemayou et al., 2012; Bartole et al. 2019; Obrist-Farner et al., 2020) based on interpretations of the migration Lake Izabal basin depocenter and other evidence. Fault switch activity between the PF and MF has been suggested by Burkart (1994), Rogers & Mann (2007), Authemayou et al. (2012), and Obrist-Farner et al., (2020). The implication is that the PF was more active in the geologic past, and even in the present has a history of significant seismic activity, including the 1785 and 1816 earthquakes, as well as several recent small earthquakes (Figure. 1.2).

The JOF zone is located south of and sub-parallel to the MF. Although there has been seismicity near the fault, whether the earthquakes occurred on the JOF or on nearby normal faults is not certain, because several active grabens cut through it (Clemons, 1966; Dengo, 1968; Muehlberger and Ritchie, 1975; Ritchie, 1975; Gordon and Muehlberger, 1994; Franco et al., 2009). Styron et al. (2020) excludes the JOF from their compilation of active faults of Central America, because, they argue, this fault system does not show any topographic evidence of recent displacement. Recent GPS studies (Ellis et al., 2018; 2019) also do not consider JOF to be active. In this study, I will show that the JOF or another fault in that vicinity does seem to have an active strike-slip strain signal; whether this is the JOF itself or a normal fault with a strike-slip component remains to be investigated.

Guzmán-Speziale (2010) and Styron et al. (2020) also identifies the Ixcán fault, 80 km north of the PF as part of the PMFS. It has evidence of recent seismicity, but prior

geologic work that has been done to look at the slip rate or historic earthquakes on the fault is not known.

1.3. FAULTS IN CAVA

The main structure of the Central American Volcanic Arc (CAVA) system in Guatemala is the strike-slip, right-lateral Jalpatagua fault, some 70-80km long (Wunderman & Rose, 1984; Gordeon & Muehlberger, 1994; Authemayou et al. 2011; Garnier, 2020; Garnier et al., 2020), which continues to the south as the El Salvador Fault zone (ESFS) (Alvarez- Gómez, 2009; Martínez- Díaz et al., 2021). Ellis et al., (2019) indicate that displacement rate along the Jalpatagua gradually increases to the southeast, from 1.4mm/yr along its north-western end, to about 7.6 mm/yr at the El Salvador boundary. We primarily focus on the PMFS in this study; however, as I will show below, strain rates on the strike-slip faults in the CAVA are among the highest in the region. There are several volcanoes in the CAVA that intersect with areas of the highest strain rate, so it is possible that some component of the strain signals shown in this study are related to volcanic deformation and not tectonics. This is an area that will require further research in the future to disentangle.

1.4. GEODETIC STUDIES IN THE PMFS AND CAVA

Several studies of displacement measure with Global Positioning System (GPS)-based techniques have been conducted in recent years in Northern Central America (Lyon-Caën et al., 2006; Rodríguez et al., 2009; Franco et al., 2012; Authemayou et al., 2012; Ellis et al., 2018, 2019; Alvarez-Gómez et al., 2019; Garnier, 2020; Legrand et al., 2020).

Lyon-Caën et al., (2006) observed a differential near-field displacement along the MF: 20mm/yr in eastern Guatemala, 12mm/yr in central Guatemala, and 8mm/yr in western Guatemala. Franco et al., (2012) found a decrease along the MF, from 18 to 22 mm/yr in eastern Guatemala, to 14-20 mm/yr in the central region, to just a few mm/yr in western Guatemala. Ellis et al. (2019) used more than 200 GPS stations in the area and determined that displacement along the MF decreases from East to West from 14mm/yr in eastern Guatemala, to 9 mm/yr in the central part, to less than 2 mm/yr at the western terminus of the fault, next to the Guatemala City graben.

According to these previous studies, the PF accommodates only 25 % (~5mm/yr) or less of the total 20 mm/yr plate boundary motion (Lyon-Caen et al., 2006; Franco et al., 2012; Ellis et al., 2019). In addition, no geodetic studies consider the Ixcán or Jocotán faults and whether they accommodate any of the plate boundary motion. This is partly due to the sparse spatial density of GNSS observations in the region, which precludes being able to resolve slip on multiple closely spaced, sub-parallel faults. There are also errors associated with the horizontal velocities of the GNSS stations, particularly because these stations are primarily campaign measurements that have all been acquired after the 1976 Motagua earthquake. It is unknown but possible that viscoelastic deformation may be contributing to errors in the GNSS velocities.

Along CAVA, Ellis et al. 2019, observed a displacement of 7.6 mm/yr in the vicinity of the Guatemala- El Salvador border, decreasing to about 2-3 mm/yr, or less, near the northwestern terminus of the fault zone. Along the Cocos-Caribbean plate convergence zone, Garnier et al. (2020) estimated a displacement of 7.1 mm/yr while Ellis et al. (2019) concluded a change in the coupling: near the Mexico-Guatemala border, locking decreases

from moderate to high and to low offshore Guatemala proper. Some authors (e.g., Álvarez-Gómez et al., 2019) consider the main fault of the CAVA, the Jalpatagua fault, to be the boundary between the forearc sliver and the CA.

1.5. RESEARCH OBJECTIVES AND QUESTIONS

Due to the lack of geodetic and paleo seismic data to constrain fault slip rates on the PMFS and other faults in the triple junction area, this study uses geodetic data to calculate surface strain rates everywhere in Guatemala, corresponding moment rates, and their uncertainties. This is done by applying a combination of different strain rate methods to estimate the strain rates, and by using MCMC to estimate fault slip rates and locking depths on the faults in the PMFS. The main objectives of the study are to:

- Quantify strain accumulation rate with its uncertainty in the region around the PMFS and the CAVA using different interpolation methods, and
- Model faults slip rates and locking depths on the faults in the eastern PMFS using the strain rate observations, calculating uncertainties by using strain profiles from the different methods and MCMC to generate a suite of parameter realizations that fit the observations.

From these results, the following research questions can be addressed:

- Which faults are active?
- What are the implied moment accumulation rates of the faults in the region and how does this compare to previous studies and historic seismicity?
- What are the implications for seismic hazard?

The following will outline the different methods used in this study, then show strain rates and strain profiles. It will show how predicted strain rates on the MF suggest around 50% of the total plate motion is accommodated on that fault, and that the total moment rate for the region matches that of historic seismicity well, at least for the PMFS. Finally, it will conclude by discussing the implications for understanding the fault system and provide some suggestions for future work.

2. DATA AND METHODS

2.1. GNSS DATA

There were 215 GPS sites in northern central America and southern Mexico. These data included both continuous and campaign data from Ellis et al, 2018.(Figure 1.2 and Figure 2.1) Daily GPS RINEX files from 74 continuous and 141 campaign GPS sites were used, including all sites in Belize, El Salvador, Guatemala, Honduras, the Mexican states of Chapas, the western portion of the Caribbean Sea, and some stations in Nicaragua. The campaign observations include some or all data from DeMets (2000, 2004,2007a,b, 2008a,b, 2009, 2011a,b,c), DeMets &Tikoff (2015a,b,c,d,e,f,g,h), Dixon (2001, 2003, 2004,2010), Franco et al. (2012), LaFemina(2013a,b,c,d,e), Lyon-Caen et al. (2006), Newman(2010), Schwartz & Dixon (2000), and Staller et al. (2016). The earliest GPS data for the study area are from 1999, although observations at several sites on the Caribbean plate or nearby areas of the North American plate extend back to 1993. 70% of the GPS sites in the study area became operational before the May 2009 Swan Islands earthquakes. GNSS data used in this study were processed by Ellis et al. 2019.

2.2. GNSS-BASED STRAIN RATES

Space-based geodesy provides a direct means of measuring surface strain rates (Ward 1994, Shen et al. 1996, Shen- Tu et al. 1999, Kreemer et al. 2000, Beavan & Haines 2001, Shen et al. 2007, Wu et al. 2011, Haines and Wallace 2020). Strain rates have been linked to the frequency of seismic events and the rate at which seismic energy accumulates-moment accumulation (Kostrov 1974, Savage and Simpson 1997, Stevens and Avouac

2016, Wu et al. 2021). Strain rates constrain seismic hazard through both identification of active faults and estimation of the moment accumulation rate (Maurer et al., 2018; Maurer and Materna, 2023).

To use geodetic data to successfully estimate surface strain rates, interpolation is required at every point in space. Numerous methods and algorithms have been established, but the study will explore the differences between the methods using a systematic approach, where the same data and query grid is used to calculate strain rates using several different methods. The earliest interpolation studies used discrete GPS observations directly to obtain a spatially continuous horizontal velocity field and strain rate (Frank, 1966; Shen et al., 1996). Maurer & Materna 2023 reviewed methodologies for strain estimation in 2D and compared a suite of methods in Southern California. They included a new implementation based on Kriging. This compared variation between methods with the uncertainties associated with the different methods. Sandwell et al., 2013 compared four interseismic velocity models of the San Andreas Fault based on GPS observations. They evaluated the mean and standard deviation these interseismic models showing the velocity models are coherent at wavelengths greater than 15-40km.

In previous studies, GNSS velocities are used to constrain slip on model faults. Ellis et al., (2019) used TEFNODE finite element modeling to calculate strain rates. Sun (2020) used a 2D finite element model to analyze the different roles of faults by testing structure geometry and simulating the PMFS. In contrast, direct estimation of strain rate makes no assumptions of a fault and does not need to solve for fault slip rates and locking depths when characterizing the strain field.

This study makes use GNSS velocities from Ellis et al., 2019, using only the horizontal components to calculate the strain rates. The tensors are then used to calculate the different invariants such as the trace of the strain rate tensor (dilation rate), the second invariant, and the maximum shear strain rate. Total moment deficit rate were calculated based on Kostrov-type summation (Savage & Simpson, 1997), which can be used to estimate the return period of a seismic event of given magnitude, or the magnitude of a future event given a time since the last. Finally, fault slip rate were modeled using 2D (anti-plane strain) elastic half-space dislocation models (e.g., Matthews and Segall, 1993).

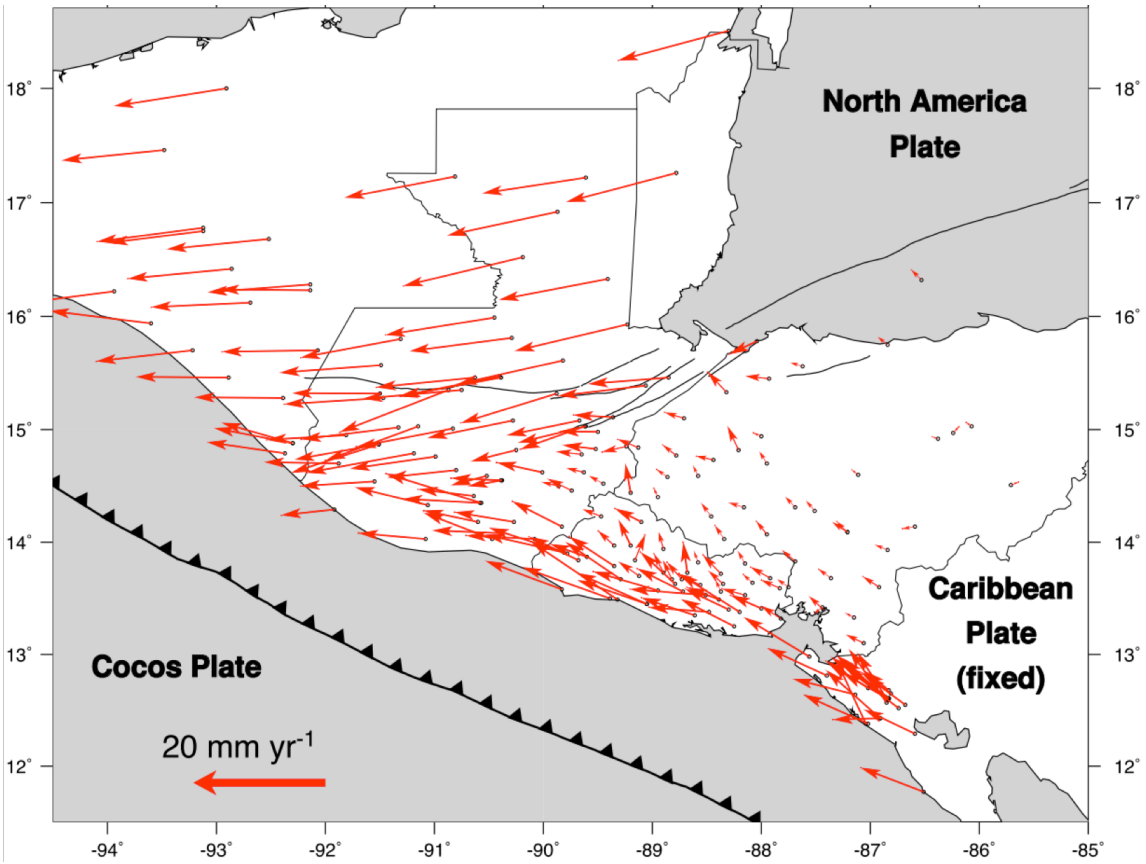

Figure 2.1. GPS site velocities from Ellis et al., (2019) relative to the CA plate corrected for coseismal offsets and transient after slip from 2009 Swan Island earthquake and the 2012 El Salvador and southern Guatemala earthquake. (Ellis et al., 2019).

2.3. STRAIN RATE CALCULATION

For 2D surfaces, determining the strain rate at each spatial point necessitates employing some form of interpolation scheme. There are several broad classes to calculate strain rates proposed by various researchers (mentioned in Methods section). The open-source python package, Strain_2D (Maurer & Materna, 2023) compiles these various classes and the different methods within it. The methods may use interpolation or additional parameterization or may directly solve for strain rates. All the methods use the same GPS velocities fields with the same grid spacing.

2.3.1. Strain_2D Data Formatting and Configuration. Strain_2D (Maurer and Materna, 2023), uses a text file. They must be space-separated table with format as follows:

 # lon(deg) lat(deg) Ve(mm) Vn(mm) Vu(mm) Se(mm) Sn(mm) Su(mm) name(optional)

```
# Format: Lon Lat Ve Vn Vu Se Sn Su ID
-89.833 13.575 -0.2 8.8 0.0 -0.4 -0.4 100 ACAJ
-89.68299999999999 13.836 3.8 8.1 0.0 -2.4 -1.4 100 AGLA
-89.80799999999999 13.909 -0.8 7.2 0.0 -0.6 -0.6 100 AHUA
-89.05 13.447 0.9 8.4 0.0 -0.5 -0.6 100 AIES
-87.999 13.405 6.8 7.2 0.0 -2.5 -1.8 100 AMAT
```

Figure 2.2 Snippet of the text file for the data utilized and included in the calculation of all the strain rates in Strain_2D package.

In the Strain_2D package, before applying a method, one must specify the area around which the interpolation is to be calculated and the grid spacing. In this study, a grid spacing of 0.04x 0.04 was taken for all the methods used (mentioned in Methods section). Within the direct computation through baselines, Delaunay triangulation (Kreemer et al., 2014) was implemented. For utilizing basis functions from elasticity, *gpsgridder* (Sandwell

&Wessel, 2016) was used. And finally, for spatial weighting functions, Local Average Gradient (Huang et al., 2022) and Geostatistical Method was used (Maurer & Materna, 2023).

2.3.2. Effect of Smoothing. All interpolation methods implement some form of smoothing, either through the choice of basic functions or through explicit penalization of gradients (Maurer & Materna, 2023). Interpolation itself introduces uncertainties due to this issue with smoothing when dealing with sparsely distributed data. Spatial smoothing affects the spatial affects the interpolated strain rates, and correctly choosing the degree of smoothing allows for a more detailed recovery of the true underlying velocity field. Smoothing should balance the need for spatial resolution with the available data density. Too smooth will mask true signals, while too rough may amplify noise. In tectonic investigations, a ubiquitous approach is to use an 'L-curve'. An L curve depicts the trade-off between how true the model is when aligned to the observed data and to some measure of the model's smoothness norm (Hansen 1992).

While interpreting an L-curve, the general anticipation is that the strain rates induced by tectonic deformation, including but not limited to fault locking or fault slipping, must be relative smoothness and long-wavelength. Conversely, rougher solutions will have better fits (ie., lower misfits) but may correspond to strain rate maps with relatively more noise. Consequently, overly smooth solutions are less likely to align well with the observed data and have greater misfits.

In order to explore the parameter space for each strain method employed in the study, a series of l-curves were generated, and the outcomes were quantified. Input velocity fields and grid spacing were kept constant for each model run. Figure 2.3 displays the L-

curve diagram comparing the misfits to the overall moment. The misfits and moment for the evaluated methods were calculated using equation (vi) and equation (xi) respectively. In Figure 2.3, the total moment rate, or the Kostrov-Summation Moment in nanostrain per year is represented on the X-axis. The assumptions are a 30GPa shear modulus, a seismographic depth of 11km, and only considers land-based strain. Data misfit on the other hand is represented in the Y-axis. It is calculated by interpolating the 0.04 ° x 0.04° gridded velocity field to that of the actual data points: utilizing the nearest neighbor method. Since the median reduced chi-square is used as the misfit metric.

$$\sigma = median\left\{\left(\frac{v_{obs}-v_{pred}}{\sigma_{obs}}\right)^2\right\} \quad \text{(xi)}$$

There is not a consistent trade-off between moment and misfit when comparing across different methods, in contrast to individual methods. Geostatistical Method has a lower misfit than local average gradient and comparable misfit to *gpsgridder.* The moment disparity is roughly 40% across all methodologies, and the misfit display about a 50% variance. These attributes stem from the systematic relocation of the L-curve in the misfit-moment domain, associated with the chosen strain rate or velocity field parameterizations of each method. This observation is underscored when comparing the geostatistical method-gaussian model to the geostatistical method-exponential method. The pair are fundamentally identical but differ in the parameterization of the velocity field using an exponential or gaussian spatial structure function.

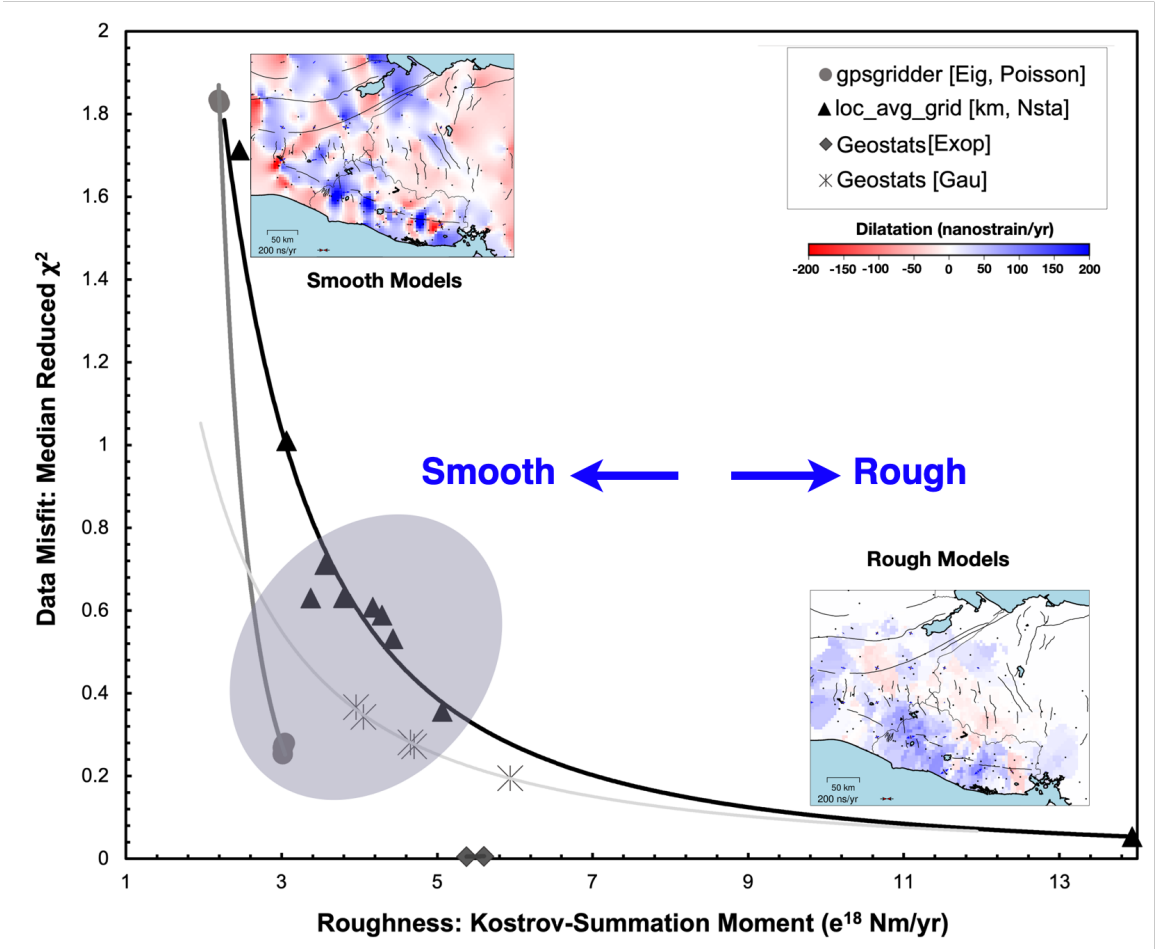

Figure 2.3 Data misfit vs total moment foreach method. Models positioned near the L-curve corners of each method, inside the grey ellipse, were chosen for further examination.

2.4. STRAIN RATE FOR SEISMIC HAZARD

The surface strain rate tensor is a symmetric, positive-definite tensor with three independent components represented by:

$$\dot{\varepsilon}_{IJ} = 0.5\left(\frac{\partial v_i}{\partial x_j} + \frac{\partial v_j}{\partial x_i}\right) \quad \text{(i)}$$

where i and j represent components of coordinates x and velocities v, respectively. Here, we focus on surface strain rates, so $i, j = 1,2$. The principal strain rates $\dot{\varepsilon}_1$ and $\dot{\varepsilon}_2$ are given by the eigenvalues of strain rate tensor:

$$\dot{\varepsilon}_1, \dot{\varepsilon}_2 = \frac{(\dot{\varepsilon}_{11} + \dot{\varepsilon}_{22})}{2} \pm \sqrt{\left(\frac{\dot{\varepsilon}_{11} - \dot{\varepsilon}_{22}}{2}\right)^2 + \dot{\varepsilon}_{12}{}^2} \quad \text{(ii)}$$

Because strain rate is a tensor, invariants are often used for plotting. Of particular importance are the trace of the strain rate tensor, which is defined as the areal strain rate or dilatation rate (rate of change in area):

$$\dot{\Delta} A = \left(\dot{\varepsilon}_{11} + \dot{\varepsilon}_{22}\right) = \dot{\varepsilon}_1 + \dot{\varepsilon}_2 \quad \text{(iii)}$$

The maximum shear strain rate:

$$\dot{\tau} = \frac{1}{2}\sqrt{\left(\dot{\varepsilon}_{11} - \dot{\varepsilon}_{22}\right)^2 + 4\dot{\varepsilon}_{12}^2} = \frac{1}{2}\left(\dot{\varepsilon}_1 - \dot{\varepsilon}_2\right) \quad \text{(iv)}$$

And the second invariant, a measure of overall magnitude of strain:

$$I_2 = \frac{1}{2}\left[\left(\dot{\varepsilon}_{11} * \dot{\varepsilon}_{22}\right) - \dot{\varepsilon}_{12}^2\right] \quad \text{(v)}$$

with the goal of relating strain rate to seismic hazard, Savage & Simpson (1997) derived a relation between the strain rate and the minimum seismic moment accumulation rate assuming a fixed seismographic depth H and shear modulus G. Based on Kostov (1974):

$$M_d \geq 2G\,\dot{H}\,A_s\left|\dot{\varepsilon}^{max}\right| \quad \text{(vi)}$$

where A_s is the area at the surface of the crustal volume considered and

$$\left|\dot{\varepsilon}^{max}\right| = \max\left\{\left|\dot{\varepsilon}_1\right|, \left|\dot{\varepsilon}_2\right|, \left|\dot{\varepsilon}_1 + \dot{\varepsilon}_2\right|\right\} \quad \text{(vii)}$$

is called ‘maximum principal strain rate’. Eq (vi) provides a lower bound on the seismic moment accumulation rate (Savage & Simpson 1997).

2.5. STRAIN RATE INTERPOLATION

Several methods for calculating strain rate tensors were used in this study using Strain_2D (Maurer & Materna 2023). This package was coded and designed to facilitate seamless interpolation of data onto the same grid for any of the implemented methods. The software outputs interpolated velocity fields, strain rate components, invariants, stand deviations, misfits, and each of their corresponding plots. Strain_2D offers command-line tools, namely 'strain_rate_compute.py' and 'strain_rate_comparison.py', for strain rate calculations. In order to determine the strain rate at every point in space requires some form of interpolation scheme. The Strain_2D package contains various interpolation methods, including direct strain rate calculation using baselines, spatial basis functions, elasticity-based techniques, and weighted neighborhood methods. With the various methods available. To estimate the optimal parameters for each approach, we used an L-curve (Figure 2.3) (Maurer & Materna, 2023). We used the following strain rate methods: Direct Strain Rate Calculation using Baselines, an elasticity-based method called *gpsgridder* (Sandwell & Wessel, 2016), a moving window method (Huang et al., 2022), and kriging (Maurer & Materna, 2023). For GNSS velocities, two separate systems are employed to solve for the two horizontal velocity components, which are then combined to calculate numerical derivatives and strain rates.

2.5.1. Elasticity-based Methods. Strain_2D utilizes the *gpsgridder* method introduced by Sandwell and Wessel (2016). This method relies on principles from elasticity and employs a 2-D thin-plate approximation to interpolate 2-D vector data (Haines et al. 2015). The application of elasticity constraints offers a physical foundation for determining the spatial correlation length scale and establishes a connection between the two horizontal

velocity components, dependent on Poisson's ratio. By applying horizontal body forces at specified locations, the surface is deformed, and these forces are optimized to match the observed surface velocities.

2.5.2. Weighted Neighborhood Methods. Strain_2D employs an ordinary kriging technique. In this category of methods, a specific local region is defined around the point being estimated, and within this region, either a weighted mean or local weighted linear least squares method is applied to estimate the velocity at target location. The weighted average process can be expressed as follows:

$$v^*(x_i) = \sum_j w_j \, v\left(x_j\right) \tag{viii}$$

where $v\left(x_j\right)$ are the observed velocities, w_j are weights assigned to each velocity, and $v^*(x_i)$ is the estimated velocity at the unobserved location x_i. Handwerger et al. (2019) and Huang et al. (2022) adopt one approach by using a moving window with a fixed radius, but they don't introduce any additional weighting for the data.

For kriging, the objective is to determine the weights w_j, in a way that the computed velocities accurately represent the spatial associations found in the observed data. This overarching category of techniques includes various variants, one of which is the nearest-neighbor approach, where all weights are set to zero except for the nearest point, which is assigned a weight of one. Utilizing spatial covariance, this evolves into the classical geostatistical challenge known as kriging. Initially, a spatial structure function is established through variogram analysis or an alternative technique to calculate the covariance between pairs of observations (Matheron et al. 1962). This structure function is then employed to calculate both the covariance matrix of observations ($\sum$) and the covariance between the observations and the unsampled estimation location (σ). There are

two types of spatial structure functions we considered with the geostatistical method, the Exponential and Gaussian models. Both the models are continuous models; however, the Gaussian model is intrinsically differentiable while the Exponential model may not be. Because we assume that the underlying velocity field must be differentiable we use the Guassian structure function.

Subsequently, one can directly compute the optimal weights w using these covariances. These optimal weights are derived through the application of ordinary kriging equations (Wackernagel 2003; Chilès & Delfiner 2012) to find the optimal weights while considering an unknown mean.

$$\begin{bmatrix} \Sigma & 1 \\ 1^T & 0 \end{bmatrix} \begin{bmatrix} \lambda \\ v \end{bmatrix} = \begin{bmatrix} \sigma_0 \\ 1 \end{bmatrix} \tag{ix}$$

where here we use the conventional symbol λ for the vector of kriging weights, and v is a Lagrange multiplier. Eq(ix) is derived by assuming a solution in the form of Eq(ix) while ensuring that it is unbiased and minimizes estimation variance. Because it is a positive semi-definite matrix, Eq(ix) can be directly inverted to solve λ and v. The weights obtained are then inserted into Eq(ix) to make predictions at the new location x_i.

2.5.3. Direct Calculation Through Baselines. The primarily focus is on interpolation-based strain rate estimation methods, but the Delaunay triangulation method allows for direct strain rate comparison at groups of three stations that form a triangle. Baselines measure the changes in the distance between two monitoring stations and directly compute strain rate. This approach is beneficial as it is relatively straightforward to calculate and does not require any additional parameters/variables for estimation. That is also precisely why this technique is highly susceptible to any noise in the observations due

to a lack of data redundancy (Kreemer et al. 2018). It is important to note that strain rates remain constant within each triangle. This makes the strain rate maps highly discretized (Figure 3.1). It also reflects the specific geometry of the monitoring station layout. Wu et al (2011) brought to attention that without any noise mitigation, Delaunay triangulation results in significant degradation of the underlying signal. The use Delaunay triangulation was for comparison purposes to the other methods, particularly for the dilatation rate as these tend to be noisy even with interpolation.

An adaptation of the Delaunay method was introduced by Kreemer et al. (2018) wherein, a hierarchy of triangles is centered around the estimation point. In this version, triangles with favorable geometric properties are retained while others are discarded. This is done to ensure the triangles are not excessively thin or skewed. These selected triangles must also be performed for each triangle, and the median values taken from the set of resulting strain rates to establish the final strain rate estimation. This approach automatically adapts to the network configuration within each triangle.

2.6. FAULT SLIP RATES AND LOCKING DEPTHS FROM PROFILES

Fault slip rate is a measure of how fast two sides of a geological fault are moving relative to one another. It is usually expressed in terms of millimeters per year (mm/yr) or centimeters per year (cm/yr). The slip rates in this research is in millimeters per year. In plate tectonics, they offer insights into the movement rates of tectonic plates. Given that plate tectonics are constantly shifting, albeit slowly, understanding their relative movements is crucial for predicting future seismic events. Ina more regional scale, determining slip rates of faults, geologists can better assess the potential earthquake hazard

of a region. Further, comparing current slip rates to geologically derived rates from the past can offer insights into how tectonic processes have evolved over time.

Locking depth of a fault refers to the depth below the Earth's surface where two sides of a fault are 'locked' together, preventing them from sliding past each other. Above this depth, the fault is locked and accumulates stress; below it, the fault can slip steadily and aseismically. As per the definition, stress accumulating takes place in the region above the locking depth which eventually releases in the form of a seismic event. Hence, understanding where the locking depth is on a particular fault can help predict the magnitude and a rough estimate of the location of future events.

To calculate the slip rates and locking depths in the Motagua, Polochic, and Jocotán faults in the two profiles AA' and BB' in Figure 3.2, slip rates, locking depth, observation points, and distance from the origin were fitted into an antiplane strike-slip fault model which returned antiplane strain rates. It must be noted that numerous models can fit into the antiplane strike slip fault model, however, prior knowledge of the study area, geological slip rates have helped to narrow down the possible slip rates and locking depths of the Motagua, Polochic, and Jocotan faults depicted in the profiles in Figure 3.2.

3. RESULTS

3.1. STRAIN RATES FROM GNSS

Utilizing the L-curve analysis, a specific group of models (marked inside the grey circle in Figure 2.3) can be identified as representative samples from each approach (displayed in Figure 3.1). This enables one to examine their congruences and discrepancies. Table 3.1 represents the final parameter values assigned for each technique in Figure 3.1. Meanwhile, Table 3.2 outlines the cumulative moment computed through the Kostrov summation method (Kostrov 1974; Savage & Simpson 1997) and the misfit to the observations corresponding to each of the selected model.

On close inspection of all the models, maximum shear strain rates are high all along the main faults of the PMFS and the triple junction. Low levels of shear strain rates are present in areas surrounding the PMFS which includes the smaller normal faults. While it has been noted that strain rates will vary depending on the method used and the presence of GNSS stations, it is evident when we compare all the methods simultaneously in Figure 3.1. The maximum shear strain rates are largely uniform across all the methods, with the primary variations being in the smoothness of the projected field.

Out of all the methods, the Delaunay triangulation method is the simplest to compute and is seen to be the roughest model (highly discretized reflecting station geometry). This is because this method calculates strain rates directly using baseline between three adjacent GNSS stations. Since the data in Guatemala is already sparse, the triangulation does not give good interpolation results in the area. Perhaps, an area with highly dense GNSS stations will result better observations for the area. Having said that,

in the current area of interest, despite the discretized appearance the accumulation of strain in the PMFS is abundantly clear as seen in the maximum shear plot in Figure 3.1.

Similarly, strain accumulation along the PMFS can be seen on the local average gradient. Instead of relying on the velocity gradient at a single point, it averages the gradient over a local area (around a radius of 80 km and 12 stations, Table 3.1). This helps in smoothing out the data, reducing the noise, and providing a more reliable estimate of the strain rates. This averaging process has helped to mitigate the effects of outliers and provides a more stable and accurate interpolation. Therefore, it is useful in Guatemala when dealing with noisy and sparse velocity measurements.

The Geostatistical method involves analyzing the spatial correlation of the velocity data using variograms or covariance functions (Gaussian in Figure 3.1) which describes how the similarity between data points decreases with distance. Once this spatial correlation is understood, kriging was applied to estimate the velocity (therefore the strain rate) at unsampled locations as it provides a best linear unbiased estimator based on the spatial correlation structure of the data.

The *gpsgridder* on the other hand uses a gridding technique to interpolate the scattered velocity data onto a regular grid, creating a continuous field of velocity data across the region. It then calculates the strain rate tensor at each grid point. *Gpsgridder* represents smoother models as compared to the rest of the methods.

From the Figure 3.1 dilatation rate, which is the rate of change in area, a general trend of high/ positive dilatation can be seen across the faults in all the models. Dilatation rates are consistent in all four methods (even observable in Delaunay). Extension occurs

throughout the region but seems to be focused along the south. It was calculated using Eq. (iii).

The second invariant (I_2) of the strain rate tensor provides information about the magnitude of the deformation rate, regardless of the specific direction of the deformation. Using Eq.(v) in calculating the I_2 it is seen that it is greater around along the faults and the triple junction. It can also be observed across all the methods used.

The mean and standard deviation of the strain rate invariants across three models (Delaunay has been excluded as it is a very and simple model) are shown in Figure 3.4. The mean maximum strain rates reflect all the methods utilized to establish strain rate of the study area and is true to all the models, ie. strain is high along the faults and the triple junction can be seem without fail. The mean dilatation is also reflecting all the models but seems to be dominated by the geostatistical method. Even so, prominent extension can be seen in along the Jalpatagua fault. Finally, the mean I_2 of all the methods also reflects deformation along the faults especially the Jalpatagua fault and the triple junction.
While looking at the standard deviation, the maximum shear strain becomes muted but can be seen following the general trend of all the other methods. The dilation is seen to be positive throughout the study area but concentrated along the faults which means extension along these fault systems. Less deformation is noticed in the I_2 on the PMFS and more is seen in the Jalpatagua fault.

Figure 3.2 and 3.3 shows graphs depicting the maximum shear strain rates measured in nanostrain per year along profiles AA’ and BB’. The Delaunay triangulation in both the profiles has the highest variability. It flattens around the PF and the MF which could be a result of the constant strain in that region within the triangulation.

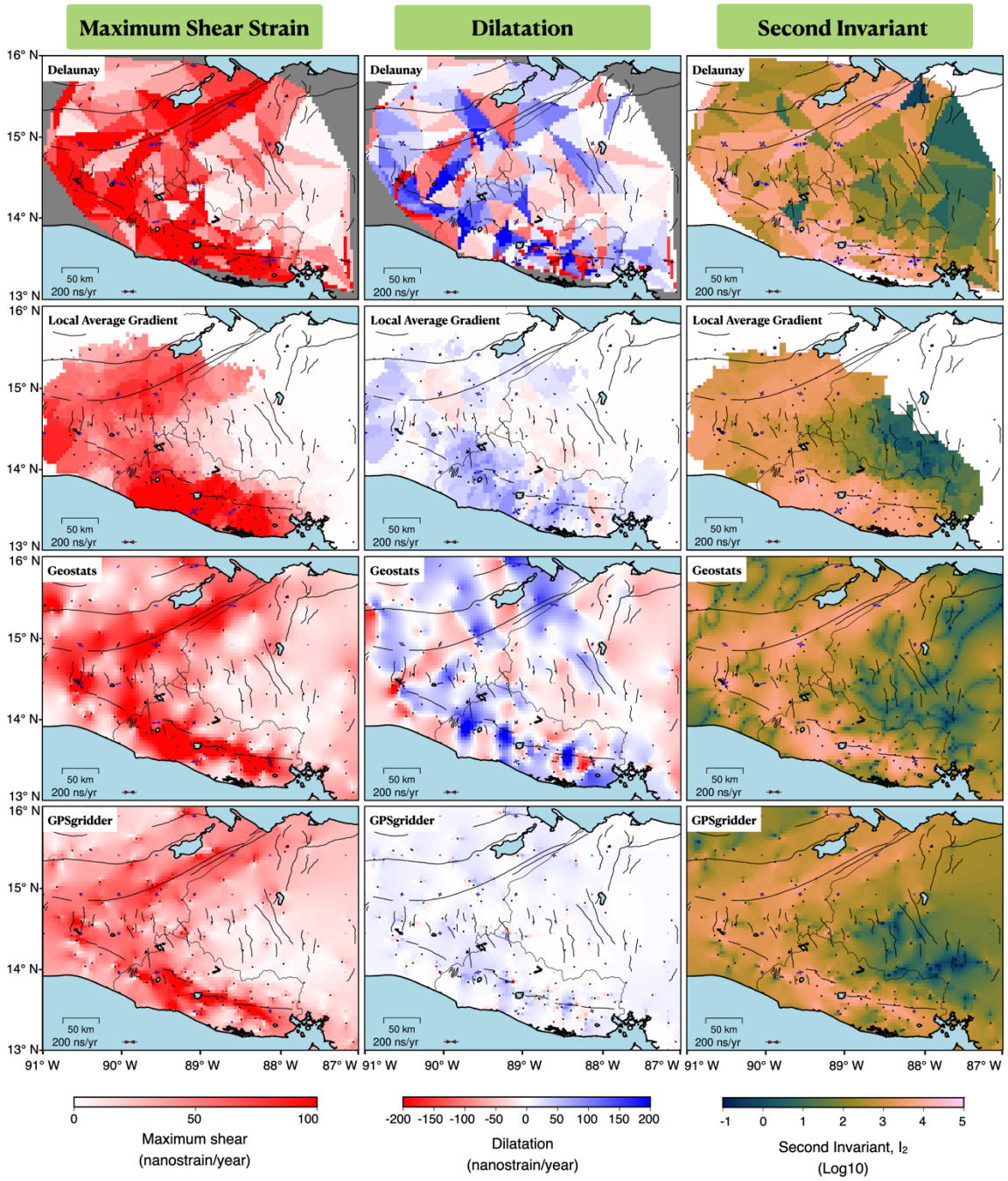

Figure 3.1 The four strain rate methods produced results for maximum shear strain rate, dilatation, and the second invariant. All the methods used the same GNSS velocities and an interpolation grid of 0.04º x 0.04º. Negative dilatation is represented by red and indicates shortening whereas positive dilatation is represented by blue and indicates lengthening.

Table 3.1 The chosen parameters for each strain rate technique in Figure 3.1. The 'Values' column displays the specific choices of these parameters, which were employed in the four strain rate methods to produce the strain rate maps depicted in Figure 3.1.

METHOD	CLASS	PARAMETERS	VALUES
All methods		Strain Range Data Range Grid size	-91.0/87.0/13.0/16.0 -91.0/87.0/13.0/16.0 0.04°/0.04°
Delaunay Triangulation (Kreemer et al., 2018)	Direct		
gpsgridder (Sandwell & Wessel 2016)	Elasticity	Poisson's Ratio Fd EigenValue	0.5 0.01 0.0005
Local Average Gradient (Huang et al., 2022)	Neighborhood	Estimate Radius (Km) Nstations	80 12
Geostatistical Method (Maurer & Materna 2023)	Neighborhood	Model Type Sill (East) Sill (North) Range (East) Range (North) Nugget (East) Nugget (North) Trend	Gaussian 1.5 1.5 0.4 0.4 0.18 0.18 0

The Delaunay is a rough model compared to others. The Local Average Gradient is also a rough model and shows a sudden jump from 0 ns/yr to almost 60ns/yr. This could be because of interpolation errors or lack of ample GNSS stations within the radius of estimation. The *gpsgridder* provides a smoother strain in both the profiles with less

variability and fewer sharp peaks. Finally, the Geostatistical methods is the smoothest model with lesser variability than the rest and shows fewer sharp peaks.

Table 3.2. Shows the integrated Kostrov moment rates (Savage and Simpson, 1997) for each of the methods. Figure 3.1 shows spatially averaged dilatation and maximum shear strain rates for each of the four methods. The moment rate distributions are calculated using a fixed geometry and shear modulus (30GPa). The real parameter values will vary spatially, but fixed spatial variations in shear modulus and depth will only influence the mean values, not the variance across different methods. The total moment rate using a locking depth of 11km has a rage of 2.8-6.78 x 10^{18}N m/yr across all the methods in the study.

METHOD	CLASS	MOMENT ACCUMULATION RATE (10^{18} N m/yr)	MEDIAN ABSOLUTE DEVIATION (mm/yr)
Delaunay Triangulation (Kreemer et al., 2018)	Direct	6.78(M_w 8)	0.00
gpsgridder (Sandwell & Wessel 2016)	Elasticity	2.88(M_w 7.75)	0.78
Local Average Gradient (Huang et al., 2022)	Neighborhood	4.72(M_w 7.90)	0.84
Geostatistical Method (Maurer & Materna 2023)	Neighborhood	4.66(M_w 7.89)	0.57

Figure 3.2 and 3.3 shows graphs depicting the maximum shear strain rates measured in nanostrain per year along profiles AA’ and BB’. The Delaunay triangulation in both the profiles has the highest variability. It flattens around the PF and the MF which

could be a result of the constant strain in that region within the triangulation. The Delaunay is a rough model compared to others. The Local Average Gradient is also a rough model and shows a sudden jump from 0 ns/yr to almost 60ns/yr. This could be because of interpolation errors or lack of ample GNSS stations within the radius of estimation. The *gpsgridder* provides a smoother strain in both the profiles with less variability and fewer sharp peaks. Finally, the Geostatistical methods is the smoothest model with lesser variability than the rest and shows fewer sharp peaks.

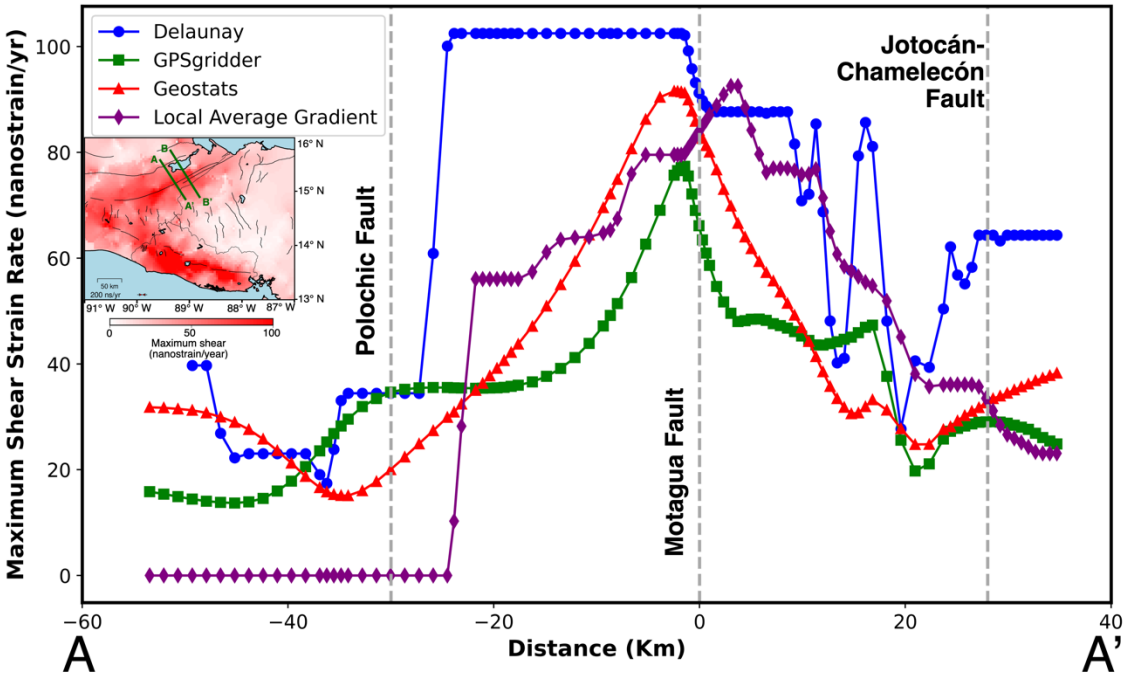

Figure 3.2. Strain Rate profiles from the four different methods along profile AA'. The reference map shows the mean maximum shear strain of all the methods except Delaunay.

The Local Average Gradient is also a rough model and shows a sudden jump from 0 ns/yr to almost 60ns/yr. This could be because of interpolation errors or lack of ample

GNSS stations within the radius of estimation. The *gpsgridder* provides a smoother strain in both the profiles with less variability and fewer sharp peaks. Finally, the Geostatistical methods is the smoothest model with lesser variability than the rest and shows fewer sharp peaks.

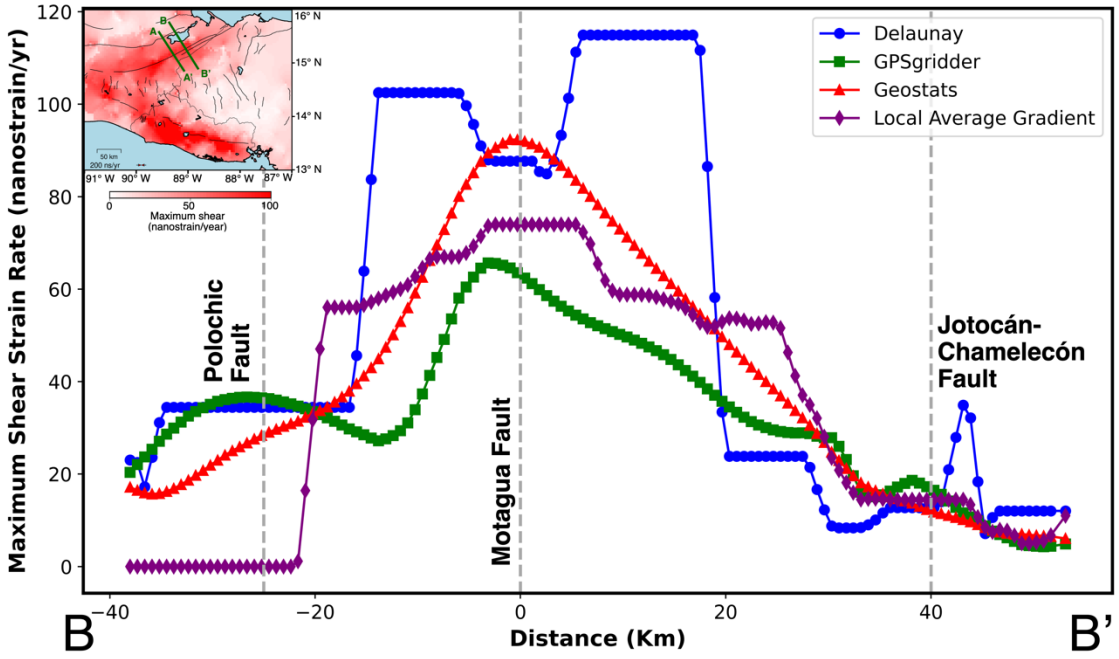

Figure 3.3. Strain rate profiles calculated from the four methods along profile BB'. The reference map shows the mean maximum shear strain of all the methods except Delaunay.

3.2. STRAIN RATE UNCERTAINTY

In geodetic studies, there are usually two types of uncertainties associated. They can either be epistemic or aleatoric. Epistemic uncertainties arise when there is a lack of knowledge of the correct Earth model to use, e.g., how many faults are active, what are the dip and depth of those faults, etc. Aleatoric uncertainty arises due to the inherently random

processes, which cannot be fully controlled for even when everything is known about a problem. Geodetic velocity observations always have a certain degree of uncertainty, which should be propagated through the estimation problem to determine how it affects the outcome. For example, given a velocity field with +/-1mm/yr uncertainties, how does that level of uncertainty translate to uncertainty in strain rate or moment?

Relating to the strain rate calculations done here, the epistemic uncertainty estimated can be related to choice of interpolation model by calculating the standard deviation of the three methods used (excluding Delaunay Triangulation). This is shown in Figure 3.4. Note that another source of epistemic uncertainty is due to the choice of hyperparameters for a given model, in this case the degree of smoothing and spatial correlation length assumed by each of the interpolation methods. In this study the L-curve method was used to choose hyperparameters (Section 3.4) because this has been used by other published studies (Maurer & Materna, 2023), but other methods could be envisioned. Considering Figure. 3.4, epistemic uncertainty tends to be high in locations where gradients in strain rates are higher than average and data are too sparse to resolve the higher variability.

3.3. FAULT SLIP RATES AND LOCKING DEPTH FROM PROFILES

Observed and predicted strain rate profiles associated with Motagua fault and the Polochic fault across the profiles shown in Figures 3.2 and 3.3 Predicted strain rate profiles were calculated using the anti-plane strain model in Segall (2010) and using an MCMC algorithm (Metropolis-Hastings, e.g. Maurer & Knight, 2014) to solve for slip rate and locking depth on the MF, PF, and JOF. Estimated fault slip rates and locking depths are

shown in Figures 3.5 & 3.6. In geophysical studies, an antiplane refers to the mode of deformation that is strictly parallel to the fault plane. These plots show histograms along the diagonal and scatter cross-plots in the off-diagonal plots of each the model parameters for the profiles AA' (Figure. 3.5) and BB' (Figure. 3.6). The histograms are the values themselves, while the cross-plots show how each variable relates to the others. There is a trade-off between parameters for a given fault; if the slip rate is low, the locking depth is also low and vice versa. The slip on the JOF (slip_j in both figures) also trades off with the slip and locking depths on the MF (slip rate indicated by slip_m and locking depth by ld_m). This is expected considering the two faults are so close to each other. This is because there is only so much slip total at the plate boundary, so if there is more slip on one fault the other accommodates the rest of the slip. The locking depth was found to be around 13.5 km for the Motagua Fault, around 35.5 km for the Polochic Fault, and 21.6km for the Jocotán Fault.

Combining the slip rates of both the profiles, the average slip rate for the MF is 6.95 mm/yr and locking depth 13.5 km. The PF has a slip rate of 3mm/yr and a locking depth of 37.5km, and finally the JOF has a slip rate of 1.6mm/yr and a locking depth of 21.6km. These are equivalent to moment rates of 0.91 $x10^{18}$ N m/yr, 1.53 $x10^{18}$ N m/yr, and 0.14 $x10^{18}$ N m/yr for the MF, PF, and JOF respectively. Considering all the faults as a single fault the moment accumulation rate is 2.58 x 10^{18} N m/yr and the corresponding earthquake magnitude is M_w 6.2 / yr. Table 3.3 shows the corresponding magnitude of the modeled moment accumulation with the Kostrov moment rates, assuming a recurrence time of 50 years.

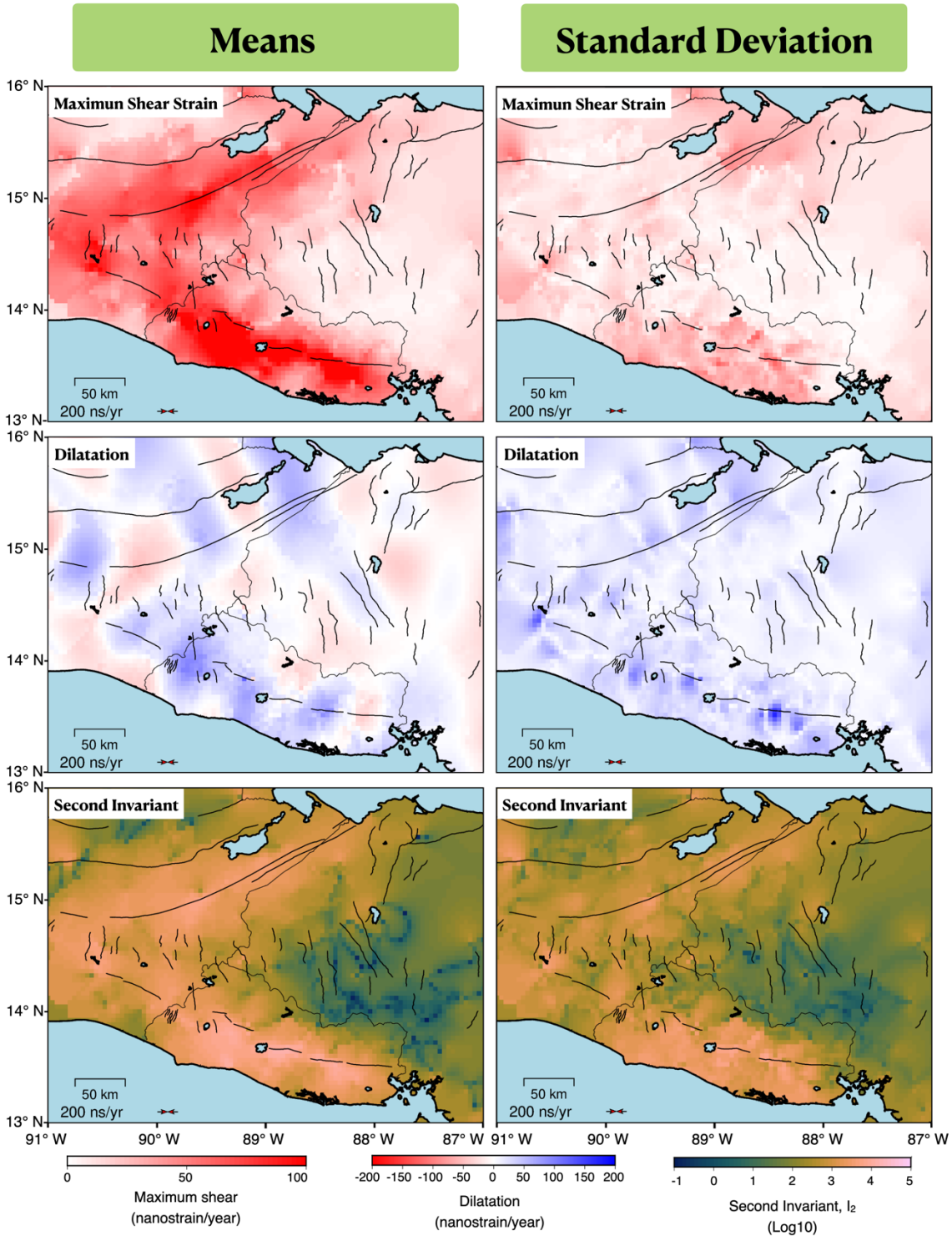

Figure 3.4 Mean and Standard Deviation derived from all methods excluding Delaunay Triangulation Method) shown in Figure 3.1. The first row shows maximum shear strain, the second row shows dilatation, and the last column represents the second invariant. Positive dilatation, represented by blue, shows extension.

For comparison, Ellis et al. (2019) assign the Motagua fault a slip rate that decreases westwards from 14±1.5 mm/yr to 9-10 ± 2mm/yr in the vicinity of the profiles shown in this study. Franco et al. (2012) also observed that the slip rates and locking depths vary along its length. In eastern Guatemala, they found a slip rate between 18–22 mm/yr, which decreases to 14–20 mm/yr in Central Guatemala. This rate further decreases to approximately 4 mm/yr in western Guatemala. They assumed a constant 20-km locking depth along the entire fault system, with a model favoring a velocity of 20 mm/yr decreasing to 16 mm/yr.

Table 3.3 Moment Accumulation Rate from Kostrov moment rates (Savage and Simpson, 1997) and modeled moment rate from the two profiles and their corresponding earthquake magnitude.

METHOD	**MOMENT ACCUMULATION RATE (10^{18} N m/yr)**	**MAGNITUDE CORRESPONDING**
Delaunay Triangulation	6.78	8.0
gpsgridder	2.88	7.75
Local Average Gradient	4.72	7.90
Geostatistical Method	4.66	7.89
Modeled	2.58	6.2

For the PF, the slip rates from Ellis et al. (2019) are based on block modeling and is ~3mm/yr. Authemayou et al., (2012) estimated a Holocene slip rate of 4.8 ± 2.3 mm/yr using cosmogenic 36Cl surface exposure dating of Quaternary volcanic markers and alluvial fans offset along the central portion of the PF. An independent geological estimated a slip rate of 2.5-3.3mm/yr based on the 25km tectonic deflection of the Chixoy River over the past 7.5-10 million years (Brocard et. al., 2011).

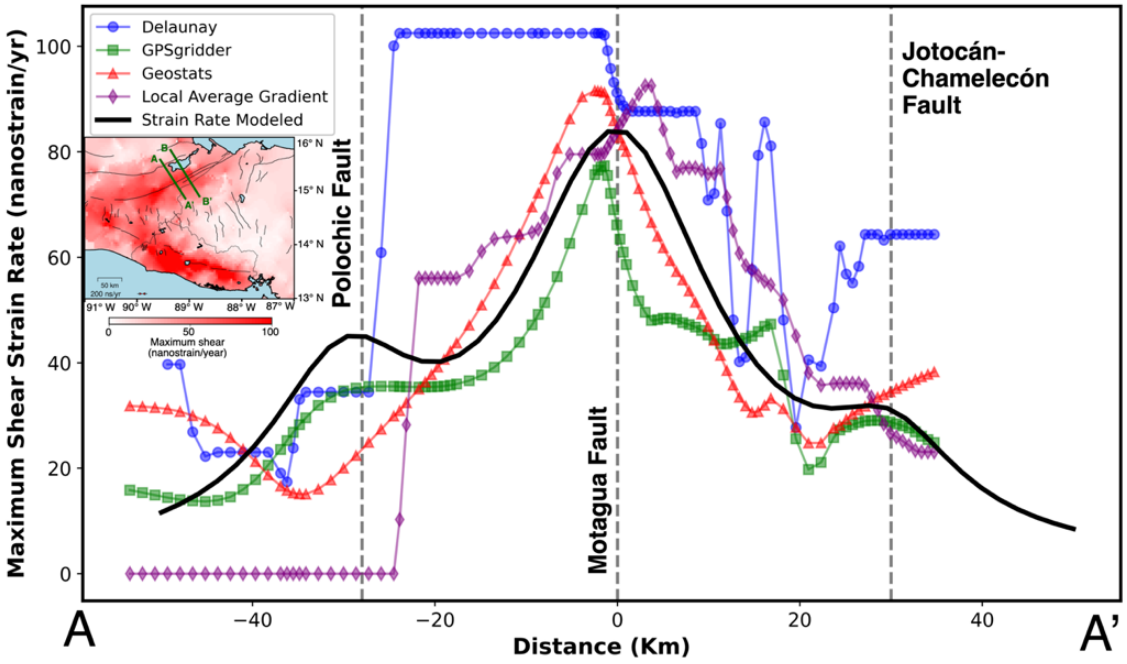

Figure 3.5. Profile along AA'. Maximum strain rate modeled using MCMC (black line) and compared with the different methods. 10^6 iterations were conducted, and the best fitting model was used. Faults are marked with the grey vertical lines along 0km (Motagua Fault), -25km (Polochic Fault), and 30km (Jocotán-Chamelecón Fault).

Figure 3.7 shows the parameters used for MF, PF, and the JOF to construct the profile in Figure 3.5. The slip rate for MF (given by slip_m) is around 4-6 mm/yr with a locking depth (ld_m) of 8-13km. Similarly, for PF the slip rate (slip_p) is found to be in

the range of 2.5-7.5mm/yr with a locking depth (ld_p) between 25-50km. Finally, for the JOF, the slip rate (slip_j) is found to be 0-5mm/yr and showed a wide range of locking depth between 0-25km.

Figure 3.8 shows the parameters used for MF, PF, and the JOF to construct the profile in figure 3.6. The slip rate for MF (given by slip_m) is around 7.5-10 mm/yr with a locking depth (ld_m) between 15-20km. Similarly, for PF the slip rate (slip_p) is found to be in the range of 0-2.5mm/yr with a wide range of locking depth (ld_p) between 0-50km. Finally, for the JOF, the slip rate (slip_j) is found to be 0-2.5mm/yr and showed a wide range of locking depth between 0-50km.

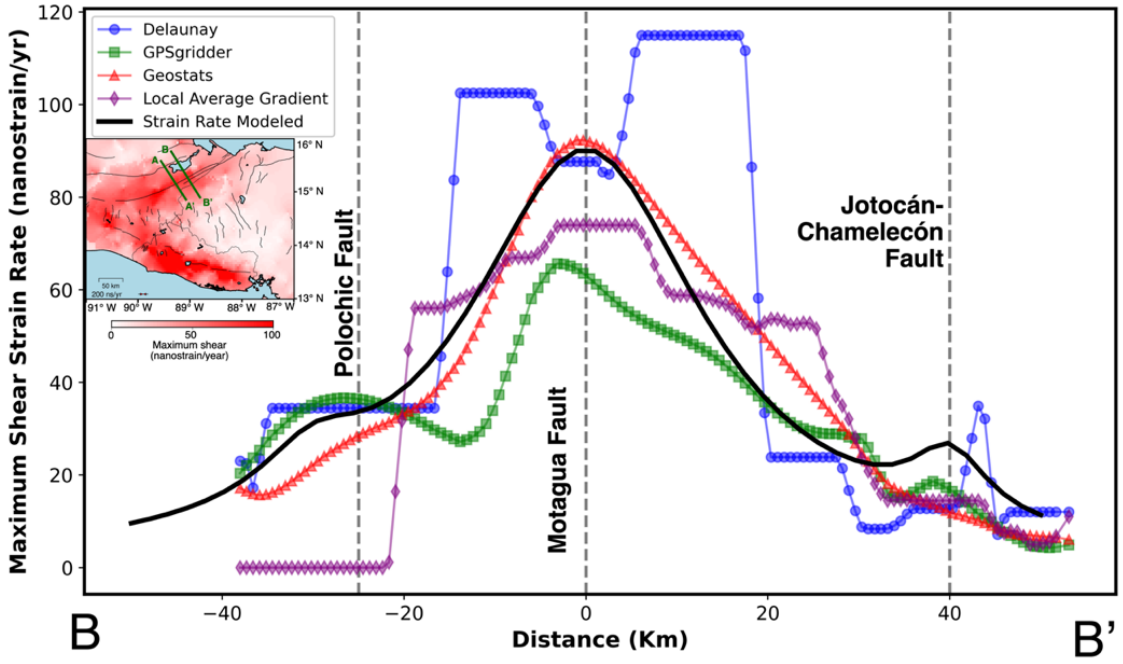

Figure 3.6 Profile along BB'. Maximum strain rate modeled using MCMC (black line) and compared with the different methods. 10^6 iterations were conducted, and the best fitting model was used. Faults are marked with the grey vertical lines along 0km (Motagua Fault), -22km (Polochic Fault), and 40km (Jocotán-Chamelecón Fault).

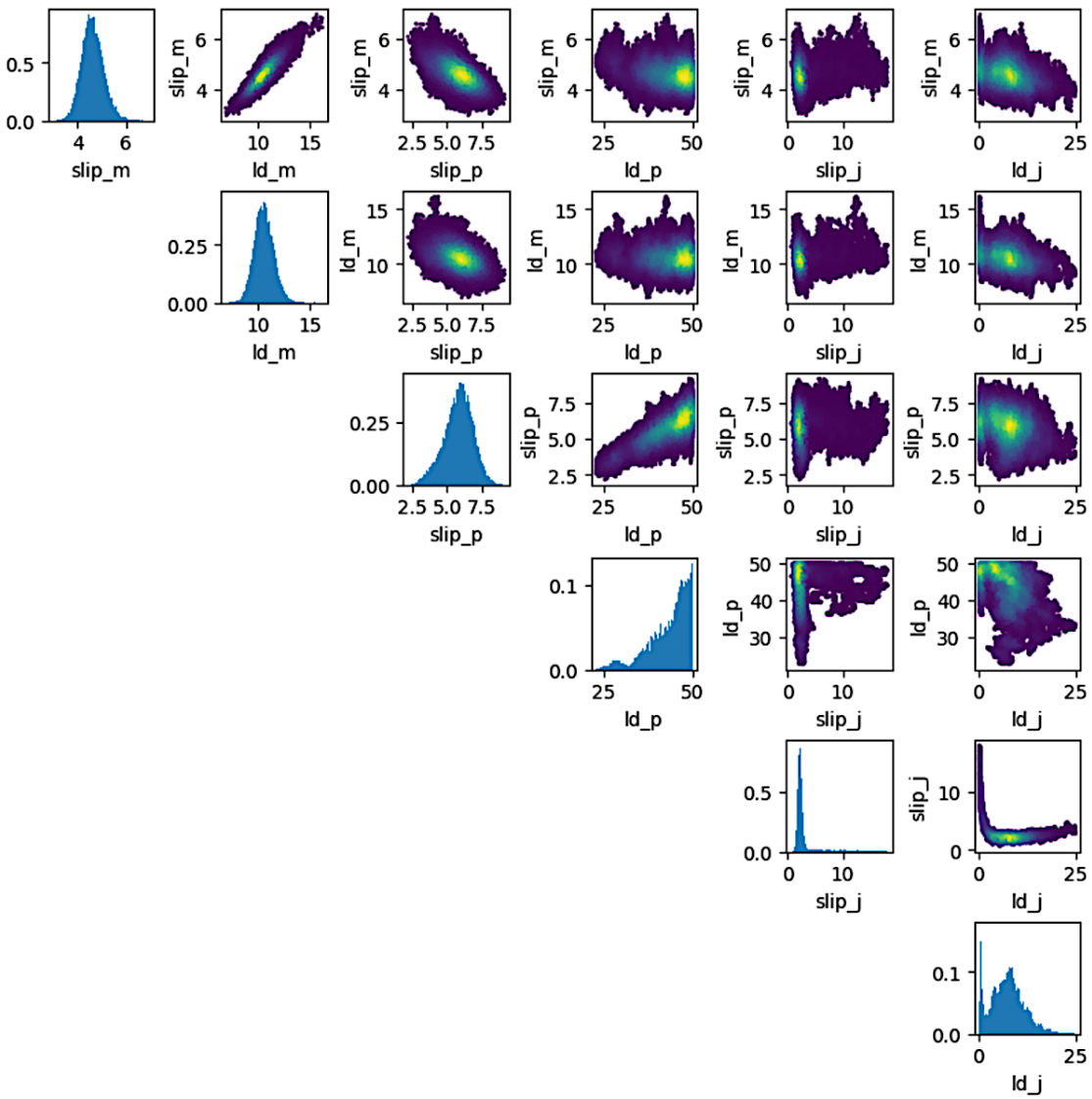

Figure 3.7 Histograms and scatter cross-plots of model parameters for profile AA' showing all values of the parameters that are allowed given the observations.

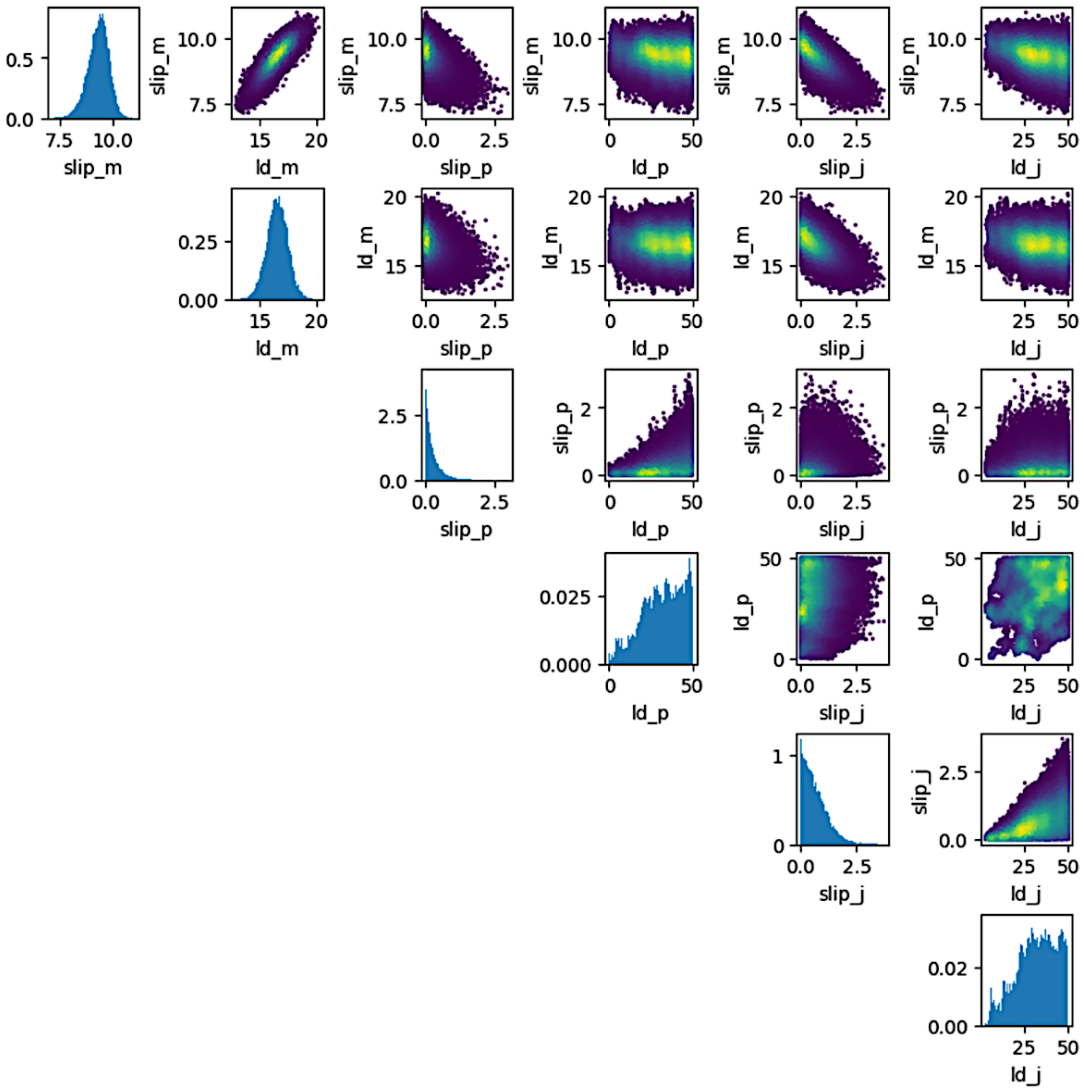

Figure 3.8 Histograms and scatter cross-plots of model parameters for profile BB' showing all values of the parameters that are allowed given the observations.

4. DISCUSSION

4.1. IMPLICATIONS FOR STRAIN RATE AND SEISMIC HAZARD IN GUATEMALA

The large-scale triple junction dynamics of the NA-CA-CO plates would normally be a subduction-subduction-transform junction, with subduction occurring between the NA and CO plates and between the CA and CO plates, and transform motion between the NA and CA plates. However, considering Figure 3.1, which shows the maximum shear strain and the dilation across all the methods, and Figure 3.4, which shows spatially averaged maximum shear strain and dilatation rates, shows that maximum strain rate is accumulating primarily along the PMFS and CAVA transform fault systems. The maximum shear strain rate in particular shows that the PMFS-Guatemala Graben-Jalpatagua Fault acts as the actual triple junction in Guatemala, marking this as a unique triple junction. Subduction is continuous across the boundary traditionally considered to be the triple junction, where the westward extension of the PF, the Tonala fault, goes offshore. Instead, transform motion is accommodated along the continental forearc "sliver" between the subduction zone and the Jalpatagua Fault and other strike-slip faults along the CAVA in Guatemala, El Salvador, and Nicaragua (Authemayou et al., 2011; Álvarez-Gómez et al., 2019). This sliver is effectively sutured to the NA plate and being translated northwest, leading to the observed strain rate distribution found in this study. As a result, the triple junction in Guatemala is effectively a transform-rift-transform junction.

It must also be taken into consideration that strain rates include contributions from various sources such as tectonics, hydrology, and magmatic systems. Strain signal seen in the JOF (Figures 3.4 and 3.6) could be related to the adjoining normal faults. Volcanism

along the Jalpatagua Fault and the ESFS influence the strain signal along the CA-CO plate boundary. For seismic hazard estimation, it is challenging to decide which non-tectonic signals to remove. Better modeling of the confounding factors is one possible approach that would potentially provide more accurate and reliable separation of tectonic strain rates from non-tectonic sources.

There is notable variability in total moment rate across the different strain rate estimation methods used in this study, with differences of about 40% observed among the three different methods (Table 3.2). Using the moment rate to estimate a re-occurrence time of a M_w 7.6 earthquake is 111.1, 67.8, and 68.6 yrs for the *gpsgridder*, Local average gradient, and geostatistical methods, respectively. These estimates are made for comparison purposes only, as they include the whole region and strain accumulating on the Jalpatagua fault as well. The Kostrov moment rates for the different methods are significantly higher than the modeled moment rates in the study because of this difference, with Kostrov moment rates giving a corresponding earthquake magnitude of ~M_W 7.9-8.0, while the moment rate based on the antiplane fault model gave a corresponding magnitude of M_w 6.2.

4.2. COMPARISON TO PREVIOUS STUDIES

Ellis et al. (2019) uses a block model to constrain the fault slip rates and corresponding locking depths. The model predictions are that the slip rates on the MF decreases westwards, from 14.2 ± 1.6 mm/yr at the fault's eastern intersection with the Swan Islands fault, decreasing to 13.0 ± 1.6 mm/yr at its intersection with the Ipala graben. The slip rate further decreases to 9.2 ± 2.2 mm/yr at the intersection with the Guatemala

City graben. West of the Guatemala City graben, the slip rate decreases rapidly from 9mm/yr to 2mm/yr or less within 50km west of the graben. Garnier et. al., (2022) discusses that across the PMFS the sinistral slip rates decreases from 11 to 13 mm/yr just north and west of the Guatemala City graben to 3mm/yr or less west of the Guatemala City graben. The slip rates along the PF also follows this trend. The locking depths estimated in the preferred model from Ellis et. al., (2019) range from 2.5-14km for the MF. The most reliable estimate of the locking depth for the MF, at a depth of 14km, is in its central region due to its well attributed GPS sites in that area. The locking depth estimates for the alternative models range from 3 to 15 km.

This preferred model (Ellis et. al., 2019) predicts slip rates of 3.1-3.3 ± 1.3 mm/yr for the PF. The estimate is more reliable for the eastern half of the fault than its western half. In the western half, earthquakes and faulting north of the fault indicate that the slip on the PF is transferred gradually northward. An alternative model from Ellis et. al., uses a deforming Chiapas block and predicts that the estimated fault slip rate decreases from 4.1mm/yr in the east to only 1.7mm/yr along the western segment of the fault. The preferred model estimates the locking depth for the PF to be consistently 5km, with a total range of 5-15km for PF. However, due to sparse GPS site coverage near both the MF and the PF in most areas and trade-offs between fault locking depths and other model parameters, the locking depths and slip rates are uncertain.

In comparison to these previous results, the average slip rate estimated in this research using the antiplane fault model is 6.95mm/yr for the eastern MF, as opposed to 13.0 ± 1.6 mm/yr predicted by Ellis et. al. For the PF, the slip rates were 3mm/yr, compared

to 3.1-3.3 ± 1.3 mm/yr (Ellis et. al., 2019). Thus, this research argues for a much lower slip rate on the MF than allowed by other previous studies.

Possible reasons for the discrepancies in slip rates seen are likely due to the different modeling assumptions made in each case. Ellis et. al., (2019) uses an elastic-kinematic block model that requires the sum of fault motion to equal the total relative plate motion, but because they only assumed two faults and did not consider the complexity of the nature of tectonics in the region, they could have misassigned too much slip to the MF. Three faults were considered in this study (the MF, the PF, and the JOF), with no requirement of matching the total plate motion rate imposed. This is likely a major contributor to the difference in results between this study and Ellis et al. and suggests that more faults than previously thought may be active in the PMFS. Other possible though less likely reasons for the discrepancy between our results could be differences in assumed bounds on slip rate or the fact that Ellis et al. use geodetic measurements in conjunction with geological and seismological data to calculate fault slip rates. However, most likely it is the model assumptions that has resulted in this large discrepancy in slip rate for the MF.

The estimated slip rates I find for the PF are like those proposed by Garnier et. al., (2022) and Ellis et. al., 2019. The best-fitting locking depths calculated for this study are 13.5 km and 37.5 km for the MF and PF, respectively, compared to 14km and 5km from Ellis et al. The locking depth for the PF is poorly constrained due to the lack of observations in the vicinity of the fault, leading to an unrealistically high locking depth.

When it comes to the JOF, most previous studies do not consider it to be an active fault. No studies have considered the JOF while analyzing slip rates in the PMFS. The model proposed in this study predicts a slip rate of 1.6mm/yr with a locking depth of

21.6km. It is important to note that the model used in this study is anti-plane strain, and as such does not account for normal faulting deformation. The strain signal seen by the different geodetic methods could possibly be related to normal faulting strain incorrectly projected into the anti-plane reference frame. However, at the least it appears that some fault around the JOF is active, potentially with a strike-slip sense of motion, and hence more attention needs to be given to the JOF in future research. Again, the locking depth is poorly constrained due to a lack of observations around the fault.

4.3. COMPARISON TO 1976 GUATEMALA EARTHQUAKE

Considering the 1976 Motagua earthquake of M_w7.6, the moment release associated with this earthquake was 2.8 x 10^{20} N m. The moment accumulation on the MF is 4.25 x 10^{17}N m/yr based on the antiplane fault modeling, which corresponds an annual earthquake of M_w 5.7. From 1976 to 2024, 48 years, the total moment to accumulate would be ~2 x 10^{19} N m, or an equivalent magnitude of M_W 6.8. Extrapolating to the time required to accumulate another M_W7.6 results in an earthquake recurrence time of 658 years. This number is at least consistent with the fact that no other large earthquakes have been observed on the MF since written records were available in Central America.

The discrepancy between the estimated magnitudes of earthquakes based on different methods in the context of moment accumulation data can once again be attributed to several factors. The physical and geological characteristics of a fault system, such as the PMFS can and is complex. Stress accumulation and release processes are dependent on factors like the length and depth of the fault, the nature of the rock as well as the history of seismic activity. Estimates based on paleo seismicity is limited by the accuracy and

completeness of the data. Further, strain accumulation may not be uniform over time or even across different sections of a fault line as shown by Ellis et al., 2019, Garnier et al., 2022, Franco et. al., 2012 etc. Certain segments might accumulate stress faster than others, or there might be periods of increased or decreased strain accumulation. Keeping all this in mind, the way data is interpreted, and the specific choices made in modeling can lead to different conclusions. The includes selection of parameters and the resolution of the models used. This makes understanding fault dynamics inherently uncertain due to the complex nature of Earth's crust and the limitations of current technology and models.

It is also worthy to note that, this estimate assumes a constant moment accumulation rate and does not account for other geological factors that might influence seismic activity. Predicting the exact timing of a future seismic event is not reliable, especially with just moment accumulation rate. Earthquake prediction involves complex set of variables and is subject to high level of uncertainty. The moment accumulation rate only gives an idea of how much seismic energy is accumulating over time in a particular region. In theory, when enough energy has accumulated, it can be released in the form of an earthquake. However, the actual occurrence of an earthquake depends on many factors, such as the geological characteristics of the region, paleo seismicity, and the behavior of nearby faults.

4.4. HOW DOES STRAIN RATE UNCERTAINTY IMPACT ESTIMATES OF SEISMIC HAZARD?

It is imperative to determine and ideally diminish uncertainties in strain rates for accurate seismic and geodetic moment rate predictions. Previous research studies in other areas have shown that uncertainty in strain rates can be 40-100%, depending on the area (Maurer & Materna, 2023; Maurer et al., 2023). There is approximately 40% discrepancy

alone amongst the three main strain rate methods used for this study. The variability between methods is primarily related to how the different methods handle spatial interpolation and depends on the choice of hyperparameters (Maurer & Materna, 2023). I used the L-curve methodology to optimize method hyperparameters, but other methods could be considered (Okazaki et al., 2021).

The analyses presented here consider uncertainties in strain rates resulting from interpolation errors but have not taken into another epistemic account: signals that are not the focus. Strain rates can be incorporated from influences like tectonic activities, water cycles, volcanic processes, and minor factors like landslides. Those harnessing strain rates for seismic risk evaluations might consider excluding non-tectonic signals before initiating the analyses. However, the optimal approach to do this remains ambiguous. For instance, max shear strain rates along the CAVA are higher even than the PMFS; however, volcanic activities could induce some of these strain signals, which would be unrelated to tectonics. For volcanoes to induce shear strain would require activities such as deformation and expansion of lava domes leading to movement along fractures, which creates high shear strain regions, particularly around the margins of lava flows. One such example is Santa Maria's Santiaguito lava dome complex (e.g., Zorn et al., 2020). Presently, no uniform strategies exist for navigating these choices, signifying a problem that warrants further exploration.

4.5. FUTURE RESEARCH DIRECTIONS

Based on the knowledge gathered while comparing strain rates in this study, a series of recommendations can be made for the use of strain rate maps in future seismic hazard models:

1. More data is needed to better constrain strain rates. In the absence of large campaigns to install and survey GNSS monuments or benchmarks, Interferometric Synthetic Aperture Radar (InSAR) observations should be integrated into standard GNSS- only strain rate analyses. There is a lack of InSAR studies in Central American countries due to the challenges with processing InSAR in tropical and mountainous regions. Only a few studies make the use of InSAR to study tectonic deformation in Central America (Consenza-Muralles et. al., 2022; Pritchard et al., 2018., García- Lanchares et. al., 2023). An InSAR-based view of interseismic deformation in Guatemala will provide a higher-resolution picture of deformation, that will shed light on the strain partitioning between the multiple sub-parallel faults in the PMFS. More work must be done to fully integrate and use InSAR with GNSS for strain rate estimation.
2. A more thorough comparison of geodetic observations with geologic and seismic observations, past and present, is recommended for future work. Comparing interseismic strain rate tensor orientations and seismic-based stress orientations could produce interesting results if done in the context of earthquake cycle modeling.

3. To reduce uncertainty in the interpolated strain rates using GNSS, data coverage and accessibility is paramount. Uncertainty in dilatation rate is particularly problematic and hence challenging to estimate. Although difficult to carry out, adding more continuous and campaign GNSS stations would be ideal to reduce these uncertainties.

5. CONCLUSION

The objective of this research was to measure the strain rates in and around Guatemala, with a particular emphasis on the Polochic-Motagua Fault System (PMFS). Employing Strain_2D, an open-source analytical tool, this study used several approaches to determine strain rates by interpolating GNSS (Global Navigation Satellite System) velocity fields. The findings regarding strain accumulation in Central America are outlined in the subsequent sections.

1. A key finding from the strain rate analyses in and around Guatemala shows that the estimated maximum shear strain rate field is nearly consistent across all applied methods. Maximum strain rate occurs along the PMFS and the CAVA. The average maximum shear strain for the Local Average Gradient, Geostatistical Method, and the *gpsgridder* are 30.92 ns/yr, 37.78 ns/yr, and 32.29 ns/yr respectively.
2. The moment accumulation rates are 6.78×10^{18}N m/yr, 2.88×10^{18}N m/yr, 4.72×10^{18}N m/yr, and 4.66×10^{18}N m/yr for Delaunay Triangulation, *gpsgridder*, Local Average gradient, and Geostatistical Method respectively. These correspond to the following earthquake magnitudes when integrated over the ~50 years since the 1976 Motagua earthquake: 8, 7.75, 7.90, and 7.89, respectively. (Note that this is using a single earthquake to represent the entire region.)
3. Methodological differences in estimating strain rates can lead to greater uncertainty than the inherent variability of each method. This underscores the

importance of using multiple strain rate methods and averaging their results, especially for seismic hazard assessment. Variability in strain rate methods arises from how they manage sparse station spacing (as can be seen in Central America) and different strain rate gradients. There is not a consistent trade-off between moment and misfit when comparing different methods. The moment disparity is roughly 40% across all methodologies.

4. Modeling using an anti-plane fault model for AA' gives a fault slip rate of 4-6 mm/yr for the MF with a locking depth of 8-13km, 2.5-7.5 mm/yr for the PF with a locking depth of 25-35 km, and 0- 5 mm/yr for the JOF with a locking depth of 0-50km. These contrast with prior published results that have a much larger slip rate on the MF.
5. Modeling using an anti-plane fault model for BB' gives a fault slip rate of 7.5-10 mm/yr for the MF with a locking depth of 15-20km, 0-2.5 mm/yr for the PF with a wide locking depth of 0-50 km, and 0-2.5 mm/yr for the JOF with a locking depth of 0-50km.

In conclusion, my results show that, by using different interpolation methods to constrain uncertainty in strain rate, moment accumulation and fault slip in Guatemala is more complex than previously considered. However, other faults in the system could also be active, contrary to what has been published previously. Strain rates can thus be used to better understand seismic hazard in the region.

BIBLIOGRAPHY

Authemayou, C., Brocard, G., Teyssier, C., Simon-Labric, T., Guttiérrez, A., Chiquín, E. N., & Morán, S. (2011). The Caribbean–North America–Cocos Triple Junction and the dynamics of the Polochic–Motagua fault systems: Pull-up and zipper models. *Tectonics*, *30*(3).

Authemayou, C., Brocard, G., Teyssier, C., Suski, B., Cosenza, B., Morán-Ical, S., González-Véliz, C. W., Aguilar-Hengstenberg, M. A., & Holliger, K. (2012). Quaternary seismo-tectonic activity of the Polochic Fault, Guatemala. *Journal of Geophysical Research: Solid Earth*, *117*(B7). https://doi.org/https://doi.org/10.1029/2012JB009444

Brocard, G., Adatte, T., Magand, O., Pfeifer, H.-R., Bettini, A., Arnaud, F., Anselmetti, F. S., & Moran-Ical, S. (2014). The recording of floods and earthquakes in Lake Chichój, Guatemala during the twentieth century. *Journal of Paleolimnology*, *52*(3), 155–169. https://doi.org/10.1007/s10933-014-9784-4

Burkart, B. (1978). Offset across the Polochic fault of Guatemala and Chiapas, Mexico. *Geology*, *6*(6), 328. https://doi.org/10.1130/0091-7613(1978)6<328:OATPFO>2.0.CO;2

Buzzanga, B., Bekaert, D. P. S., Hamlington, B. D., & Sangha, S. S. (2020). Toward Sustained Monitoring of Subsidence at the Coast Using InSAR and GPS: An Application in Hampton Roads, Virginia. *Geophysical Research Letters*, *47*(18), e2020GL090013. https://doi.org/https://doi.org/10.1029/2020GL090013

Correa-Mora, F., DeMets, C., Cabral-Cano, E., Marquez-Azua, B., & Diaz-Molina, O. (2008). Interplate coupling and transient slip along the subduction interface beneath Oaxaca, Mexico. *Geophysical Journal International*, *175*(1), 269–290. https://doi.org/10.1111/j.1365-246X.2008.03910.x

Deaton, B. C., & Burkart, B. (1984). Time of sinistral slip along the polochic fault of Guatemala. *Tectonophysics*, *102*(1–4), 297–313. https://doi.org/10.1016/0040-1951(84)90018-0

Ellis, A., DeMets, C., Briole, P., Cosenza, B., Flores, O., Graham, S. E., Guzmán-Speziale, M., Hernández, D., Kostoglodov, V., LaFemina, P., Lord, N., Lasserre, C., Lyon-Caen, H., Rodriguez Maradiaga, M., McCaffrey, R., Molina, E., Rivera, J., Rogers, R., & Staller, A. (2018). GPS constraints on deformation in northern Central America from 1999 to 2017, Part 1 – Time-dependent modelling of large regional earthquakes and their post-seismic effects. *Geophysical Journal International*, *214*(3), 2177–2194. https://doi.org/10.1093/gji/ggy249

Ellis, A., DeMets, C., McCaffrey, R., Briole, P., Cosenza Muralles, B., Flores, O., Guzmán-Speziale, M., Hernández, D., Kostoglodov, V., LaFemina, P., Lord, N., Lasserre, C., Lyon-Caen, H., Rodriguez Maradiaga, M., Molina, E., Rivera, J., Rogers, R., Staller, A., & Tikoff, B. (2019). GPS constraints on deformation in northern Central America from 1999 to 2017, Part 2: Block rotations and fault slip rates, fault locking and distributed deformation. *Geophysical Journal International*, *218*(2), 729–754. https://doi.org/10.1093/gji/ggz173

Franco, A., Lasserre, C., Lyon-Caen, H., Kostoglodov, V., Molina, E., Guzman-Speziale, M., Monterosso, D., Robles, V., Figueroa, C., Amaya, W., Barrier, E., Chiquin, L., Moran, S., Flores, O., Romero, J., Santiago, J. A., Manea, M., & Manea, V. C. (2012). Fault kinematics in northern Central America and coupling along the subduction interface of the Cocos Plate, from GPS data in Chiapas (Mexico), Guatemala and El Salvador. *Geophysical Journal International*, *189*(3), 1223–1236. https://doi.org/10.1111/j.1365-246X.2012.05390.x

García-Lanchares, C., Marchamalo-Sacristán, M., Fernández-Landa, A., Sancho, C., Krishnakumar, V., & Benito, B. (2023). Analysis of Deformation Dynamics in Guatemala City Metropolitan Area Using Persistent Scatterer Interferometry. *Remote Sensing*, *15*(17), 4207.

Garnier, B., Tikoff, B., Flores, O., Jicha, B., DeMets, C., Cosenza-Muralles, B., Hernandez, D., Marroquin, G., Mixco, L., & Hernandez, W. (2020). An integrated structural and GPS study of the Jalpatagua fault, southeastern Guatemala. *Geosphere*, *17*(1), 201–225. https://doi.org/10.1130/GES02243.1

Graham, S. E., DeMets, C., DeShon, H. R., Rogers, R., Maradiaga, M. R., Strauch, W., Wiese, K., & Hernandez, D. (2012). GPS and seismic constraints on the M = 7.3 2009 Swan Islands earthquake: implications for stress changes along the Motagua fault and other nearby faults. *Geophysical Journal International*, *190*(3), 1625–1639. https://doi.org/https://doi.org/10.1111/j.1365-246X.2012.05560.x

Guzmán-Speziale, M. (2010). Beyond the Motagua and Polochic faults: Active strike-slip faulting along the Western North America–Caribbean plate boundary zone. *Tectonophysics*, *496*(1), 17–27. https://doi.org/https://doi.org/10.1016/j.tecto.2010.10.002

Guzmán-Speziale, M., & Molina, E. (2022). Seismicity and seismically active faulting of Guatemala: A review. *Journal of South American Earth Sciences*, *115*, 103740. https://doi.org/https://doi.org/10.1016/j.jsames.2022.103740

Jicha, B. R., & Hernandez, W. (2022). Effusive and explosive eruptive history of the Ilopango caldera complex, El Salvador. *Journal of Volcanology and Geothermal Research*, *421*, 107426.

Lodolo, E., Menichetti, M., Guzmán-Speziale, M., Giunta, G., & Zanolla, C. (2009). Deep structural setting of the North American-Caribbean plate boundary in eastern Guatemala. *Geofísica Internacional*, *48*(3). https://doi.org/10.22201/igeof.00167169p.2009.48.3.25

Lyon-Caen, H., Barrier, E., Lasserre, C., Franco, A., Arzu, I., Chiquin, L., Chiquin, M., Duquesnoy, T., Flores, O., Galicia, O., Luna, J., Molina, E., Porras, O., Requena, J., Robles, V., Romero, J., & Wolf, R. (2006). Kinematics of the North American–Caribbean-Cocos plates in Central America from new GPS measurements across the Polochic-Motagua fault system. *Geophysical Research Letters*, *33*(19). https://doi.org/https://doi.org/10.1029/2006GL027694

Maurer, J., Bekaert, D. P., Sangha, S., Buzzanga, B. A., Marshak, C., Lei, Y., Kumar, P., & Fattahi, H. (2021). RAiDER: Raytracing Atmospheric Delay Estimation for RADAR. *AGU Fall Meeting 2021,* G44A-07.

Maurer, J., Materna, K. (2023). Quantification of geodetic. Strain rate uncertainties and implications for seismic hazard estimates. *Geophysical Journal International 234(3)*.

Obrist-Farner, J., Eckert, A., Locmelis, M., Crowley, J. L., Mota-Vidaure, B., Lodolo, E., Rosenfeld, J., & Duarte, E. (2020). The role of the Polochic Fault as part of the North American and Caribbean Plate boundary: Insights from the infill of the Lake Izabal Basin. *Basin Research*, *32*(6), 1347–1364. https://doi.org/https://doi.org/10.1111/bre.12431

Plafker, G. (1976). Tectonic Aspects of the Guatemala Earthquake of 4 February 1976. *Science*, *193*(4259), 1201–1208. https://doi.org/10.1126/science.193.4259.1201

Pritchard, M. E., Biggs, J., Wauthier, C., Sansosti, E., Arnold, D. W., Delgado, F., ... & Zoffoli, S. (2018). Towards coordinated regional multi-satellite InSAR volcano observations: results from the Latin America pilot project. *Journal of Applied Volcanology*, *7*(1), 1-28.

Rogers, R. D., & Mann, P. (2007). Transtensional deformation of the western Caribbean–North America plate boundary zone. In P. Mann (Ed.), *Geologic and Tectonic Development of the Caribbean Plate Boundary in Northern Central America* (Vol. 428, p. 0). Geological Society of America. https://doi.org/10.1130/2007.2428(03)

Schwartz, D. P., Cluff, L. S., & Donnelly, T. W. (1979). Quaternary Faulting Along the Caribbean–North American Plate Boundary in Central America. In C. A. WHITTEN, R. GREEN, & B. K. MEADE (Eds.), *Developments in Geotectonics* (Vol. 13, pp. 431–445). Elsevier. https://doi.org/https://doi.org/10.1016/B978-0-444-41783-1.50070-2

Styron, R., García-Pelaez, J., & Pagani, M. (2020). CCAF-DB: the Caribbean and Central American active fault database. *Nat. Hazards Earth Syst. Sci.*, *20*(3), 831–857. https://doi.org/10.5194/nhess-20-831-2020

White, R. A. (1984). *Catalog of historic seismicity in the vicinity of the Chixoy-Polochic and Motagua faults, Guatemala*.

White, R. A. (1985). The Guatemala earthquake of 1816 on the Chixoy-Polochic fault. *Bulletin of the Seismological Society of America*, *75*(2), 455–473. https://doi.org/10.1785/BSSA0750020455

White, R. A., Ligorría, J. P., & Cifuentes, I. L. (2004). Seismic history of the Middle America subduction zone along El Salvador, Guatemala, and Chiapas, Mexico: 1526–2000. In W. I. Rose, J. J. Bommer, D. L. López, M. J. Carr, & J. J. Major (Eds.), *Natural Hazards in El Salvador* (Vol. 375, p. 0). Geological Society of America. https://doi.org/10.1130/0-8137-2375-2.379

Yunjun,Z., Fattahi, H., & Amelung, F. (2019). Small baseline InSAR time series analysis: Unwrapping errir correction and noise reduction. *Computers & Geosciences, 133*, 104331. https://doi.org/10.1016/j.cageo.2019.104331

VITA

Tanaya Kashyap was born in India. She earned her bachelor's in science degree in Geology (Honors) from University of Delhi, India in July 2021. After graduation, she attended Missouri University of Science and Technology, in Rolla, Missouri for her master's degree. She started her master's program in Geology and Geophysics in August 2021, working with Dr. Jeremy Maurer and Dr. Jonathan Obrist-Farner. She received her Master of Science in Geology and Geophysics from Missouri University of Science and Technology in May 2024.